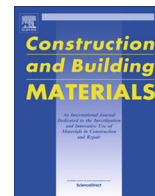




Contents lists available at ScienceDirect

Construction and Building Materials

journal homepage: www.elsevier.com/locate/conbuildmat

Mineralogical and microstructural response of hydrated cement blends to leaching



Claudia Baldermann^a, Andre Baldermann^{b,*}, Orkun Furat^c, Markus Krüger^a, Manfred Nachtnebel^d, Hartmuth Schroettner^d, Joachim Juhart^a, Volker Schmidt^c, Josef Tritthart^a

^a Institute of Technology and Testing of Building Materials (IMBT-TVFA), Graz University of Technology, Inffeldgasse 24, 8010 Graz, Austria

^b Institute of Applied Geosciences (IAG) and NaWi Graz Geocenter, Graz University of Technology, Rechbauerstraße 12, 8010 Graz, Austria

^c Institute of Stochastics, Ulm University, Helmholtzstraße 18, 89069 Ulm, Germany

^d Institute of Electron Microscopy and Nanoanalysis and Center for Electron Microscopy (FELMI-ZFE), Graz University of Technology, Steyrergasse 17, 8010 Graz, Austria

HIGHLIGHTS

- Microstructural and mineralogical alteration patterns of cement blends due to Ca-leaching and carbonation are shown.
- Conversion of portlandite to calcium carbonate has no passivation effect to the pore system.
- Ca-depletion and recrystallization of C-S-H controls the evolution of porosity and thickness of leached layer.
- Use of fine limestone powder improves the resistance against leaching and carbonation by a microfiller effect.
- Mix designs with up to 70 wt-% replacement by SCMs show equal or better performance than pure CEM 1.

ARTICLE INFO

Article history:

Received 12 April 2019

Received in revised form 9 July 2019

Accepted 5 September 2019

Keywords:

Blended cements

Supplementary cementitious materials

Corrosion

Carbonation

Porosity

Pore solution

Dissolution

C-S-H

ABSTRACT

Recent advances in concrete technology have enabled the manufacturing of hydrated cements blended with high levels of supplementary cementitious materials (SCMs). These composites can exhibit mechanical and physical properties similar to ordinary Portland-based cements; yet their equivalent performance in “corrosive” environments has to be proven. In this paper, we describe mineralogical, microstructural and geochemical alteration patterns of hydrated cement pastes, despite adequate curing, containing 10 wt-% up to 70 wt-% replacement of Portland cement by SCMs, due to combined leaching and carbonation attack for 182 days. Such knowledge is highly relevant for assessing degradation features of steel-reinforced concrete in tunnels.

The dissolution of portlandite, katoite and tobermorite as well as recrystallization of C-S-H caused the development of a leached layer around the specimen's surface. Calcite, vaterite and hydrocalcite precipitated within the altered zone, but no passivation effect due to clogging of pore space by these deposits was observed. The thickness of the altered layer, the amounts of portlandite dissolved and CaCO₃ phases neo-formed, the decrease in the Ca/Si molar ratio of C-S-H and the increase in total porosity were highest in pure cement paste. All hydrated cements blended with different types and levels of SCMs (including metakaolin, silica fume, limestone, granulated slag, and their combinations) have behaved better than the pure cement paste, which demonstrates the equivalent performance of these blended mixes in weakly aggressive environments.

© 2019 Elsevier Ltd. All rights reserved.

* Corresponding author at: Institute of Applied Geosciences, Graz University of Technology, Rechbauerstraße 12, 8010 Graz, Austria.

E-mail addresses: claudia.baldermann@tugraz.at (C. Baldermann), baldermann@tugraz.at (A. Baldermann), orkun.furat@uni-ulm.de (O. Furat), krueger@tugraz.at (M. Krüger), manfred.nachtnebel@felmi-zfe.at (M. Nachtnebel), hartmuth.schroettner@felmi-zfe.at (H. Schroettner), joachim.juhart@tugraz.at (J. Juhart), volker.schmidt@uni-ulm.de (V. Schmidt), tritthart@tugraz.at (J. Tritthart).

1. Introduction

In recent times, hydrated cements blended with supplementary cementitious materials (SCMs) are widely used for the large-scale production of concrete, owing to valuable environmental, technical and economic benefits, compared to concrete made of ordinary Portland cement (OPC) [1–5]. Specifically, cement blends that are optimized with respect to the packing density and binder

composition have been shown to exhibit a lower global warming potential ($\geq 35\%$) than OPC, while maintaining the desired workability, mechanical requirements and durability properties [5–11]. For these reasons, granulated blast furnace slag, metakaolin, fly ash and fine limestone powders among other SCMs, are nowadays substituted at different levels in concrete (e.g. 10% up to 65% for cement without other additives) [12–16]; yet the equivalent performance and durability of these mix designs in different environments (e.g. in tunnels) have to be proven.

Concrete structures are frequently subjected to different forms of physical and chemical attacks, such as leaching, carbonation, freeze–thaw and external sulfate attack [12,17–21]. Specifically, cast-in-place concrete linings, which are used in tunnels as a permanent support measure, are often exposed to so-called “soft waters”, i.e. representing poorly mineralized, natural waters (e.g. meteoric or drainage solutions) that are undersaturated with respect to (hydrated) cement phases [22]. Resultant leaching action can force the decomposition of cementitious materials and is subsequently leading to an increase of porosity and reduction of strength; thus opening the door for more deleterious attacks [19,23,24]. The response of OPC-based concrete to leaching is generally well understood; however, the (life-time) performance of hydrated cements blended with different types and levels of SCMs in weakly aggressive environments is still poorly constrained, and the mineralogical and microstructural response of such mixes to leaching not entirely understood.

It is generally accepted that the type, amount, composition and distribution of cement hydrates in the cement paste take a key control on the microstructural characteristics (total porosity, pore size distribution etc.) and durability of the hardened concrete [22]. Hence, advanced knowledge of the hydration processes in OPC is required, which may be summarized as follows: the clinker phases, i.e. alite [Ca_3SiO_5], belite [Ca_2SiO_4], tricalcium aluminate [$\text{Ca}_3\text{Al}_2\text{O}_6$], calcium aluminoferrite [$\text{Ca}_2(\text{Al,Fe})_2\text{O}_5$] and gypsum [$\text{CaSO}_4 \cdot 2\text{H}_2\text{O}$], typically react with water to form portlandite [$\text{Ca}(\text{OH})_2$], calcium silicate hydrates [C–S–H], monosulfoaluminate [$\text{Ca}_4\text{Al}_2(\text{SO}_4)(\text{OH})_{12} \cdot 6\text{H}_2\text{O}$] and ettringite [$\text{Ca}_6\text{Al}_2(\text{SO}_4)_3(\text{OH})_{12} \cdot 26\text{H}_2\text{O}$]. In the presence of limestone (micro)fillers, monocarboaluminate [$\text{Ca}_4\text{Al}_2(\text{CO}_3)(\text{OH})_{12} \cdot 5\text{H}_2\text{O}$], hemicarboaluminate [$\text{Ca}_4\text{Al}_2(\text{CO}_3)_{0.5}(\text{OH})_{13} \cdot 5.5\text{H}_2\text{O}$], hydroxyl-AFm [$\text{Ca}_4\text{Al}_2(\text{OH})_{12} \cdot 7\text{H}_2\text{O}$] or Friedel’s salt [$\text{Ca}_2\text{Al}(\text{OH})_6(\text{Cl,OH}) \cdot 2\text{H}_2\text{O}$] can also form [25–27]. Importantly, during progressive hydration, $\text{Ca}(\text{OH})_2$ can react further with SCMs to form additional C–S–H, which represents the main reaction product in fully hydrated OPC and in hydrated cement blends. The nature, composition and quantity of C–S–H in the hardened cement paste significantly contribute to the mechanical properties (i.e. early strength development) and durability of concrete structures [25,28].

The reduction of the $\text{Ca}(\text{OH})_2$ content in favor of C–S–H phase formation can accelerate steel corrosion, e.g. in concrete repairs and single shell concrete and shotcrete structures, whether mesh or fiber reinforced, especially in combination with leaching and carbonation [10,29–31]. Steel, embedded in concrete, is physically protected by the concrete layer itself and chemically by the thin passive layer that develops on the steel surface under highly alkaline conditions ($\text{pH} \sim \geq 12.5$) [22,32,33]. If the $\text{Ca}(\text{OH})_2$ content is initially reduced by the reaction with SCMs or progressively leached away from of the cement paste during interaction with soft waters, as indicated before, the pH of the pore solutions will start to decrease. Such pH drop increases the risk for the invasion of CO_2 from the atmosphere and for the uptake of dissolved inorganic carbon species from percolating groundwater; thus, speeding up the rate of carbonation front propagation from the concrete surface towards the steel reinforcement [32,34–39]. These processes, if initiated once, can rapidly shift the regime from passivation to steel corrosion.

The resistance of concrete to leaching, carbonation and steel corrosion depends mainly on the binder composition and on the microstructure, which are controlled by the mix design, type of cement and SCMs used, water/binder ratio, curing etc. [27,37,39,40]. Insufficient curing, for example, has a direct negative effect on concrete permeability and therefore on the resistance to withstand the ingress of Cl^- ions and gaseous CO_2 among other deleterious components [41,42]. The effects of these variables on the durability of hydrated cement blends have been extensively studied, but significant gaps in knowledge still persist regarding the mineralogical and microstructural response of hydrated cement blends during interaction with soft waters. In this paper, we elucidate the physicochemical controls and reaction paths leading to modifications of the microstructure, mineralogy and chemical composition of hydrated cement blends due to soft leaching attack.

2. Materials and methods

2.1. Materials, testing procedure and microstructural inspection

The mix design of the cement pastes is shown in Table 1. In detail, a reference cement paste (CEM_{100}) made from CEM I 52.5R (mean particle diameter - $d_{50} = 7.0 \mu\text{m}$) with a clinker content of $>95 \text{ wt}\%$ and C_3A content of $\sim 12 \text{ wt}\%$ was cast, according to [43]. Five cement blends were prepared by mixing the same CEM I 52.5R with different proportions and types of SCMs, such as silica fume (SF: $d_{50} = 0.3 \mu\text{m}$), metakaolin (MK: $d_{50} = 2.1 \mu\text{m}$), limestone mesofiller (MEF: $d_{50} = 5.0 \mu\text{m}$), limestone microfiller (MIF: $d_{50} = 1.2 \mu\text{m}$) and granulated slag (GS: $d_{50} = 10.9 \mu\text{m}$). These samples are labelled as $\text{CEM}_{90}/\text{SF}_{10}$, $\text{CEM}_{30}/\text{GS}_{70}$, $\text{CEM}_{90}/\text{MK}_{10}$, $\text{CEM}_{60}/\text{MEF}_{32.5}/\text{MIF}_{7.5}$ and $\text{CEM}_{60}/\text{MEF}_{32.5}/\text{MK}_{7.5}$, where the number indicates the amount of SCM substitution by $\text{wt}\%$ for CEM I. All specimens were fabricated at a constant water/binder-ratio of 0.6 (w/b-ratio, where b denotes the sum of CEM I 52.5R as well as latent-hydraulic GS, pozzolanic SF, MK and the two inert limestone powders, i.e., MEF and MIF). However, the portion of hydraulically active materials differed from 100% for CEM_{100} and blends with GS, SF and MK to only 60% for $\text{CEM}_{60}/\text{MEF}_{32.5}/\text{MIF}_{7.5}$.

The cement pastes were filled in plastic bags, which were placed in cylindrical plastic tubes (diameter of 70 mm, height of 150 mm) and rotated over night to prevent segregation. Then, the bags were extracted from the tubes, placed in a second plastic bag and stored at $20 \text{ }^\circ\text{C}$ (Fig. 1). During sample storage, the specimen’s surface was sporadically coated with a thin layer of bleed water due to an interfacial zone that developed between the plastic bag and the paste (i.e. $\sim 100\%$ relative humidity was maintained in the second plastic bag). Noteworthy, the bleed water and the pore solutions were undersaturated with respect to the partial pressure of CO_2 in atmosphere ($P_{\text{CO}_2} = 10^{-3.4} \text{ atm}$) at any time during curing, allowing atmospheric CO_2 to diffuse through the semi-permeable plastic bags, where it was converted into dissolved carbon species (mainly CO_3^{2-} , Fig. 1). In the literature, such storage conditions are often described as ideal, i.e. reducing the self-desiccation in the cement paste and keeping the material water-saturated or nearly water-saturated as long as possible in order to produce fully hydrated and hardened cement pastes without any optical signs of alteration [44,45]. Several studies [41,42] have concluded that curing is crucial for concrete (esp. with pozzolanic material) to improve its corrosion resistance, and that inadequate curing will result in poor performance.

After 28, 56, 91 and 182 days of storage in plastic bags, the packing was removed and the test specimen were placed into a steel cylinder of a special adapted hydraulic press, which squeezes the samples with a maximum load of 1300 kN/mm^2 [46,47]. The

Table 1
Mix design for the reference cement and cement blends (total volume: app. 460–470 cm³).

Sample	CEM I 52,5 R	GS	SF	MK	MEF	MIF	water	w/b
ID	[cm ³]	[-]						
CEM ₁₀₀	159.6						300.6	0.6
CEM ₃₀ /GS ₇₀	47.9	120.1					300.6	0.6
CEM ₉₀ /SF ₁₀	143.6		22.8				300.6	0.6
CEM ₉₀ /MK ₁₀	143.6			19.3			300.6	0.6
CEM ₆₀ /MEF _{32.5} /MIF _{7.5}	95.7				60.3	13.9	300.6	0.6
CEM ₆₀ /MEF _{32.5} /MK _{7.5}	95.7			15.2	60.3		300.6	0.6

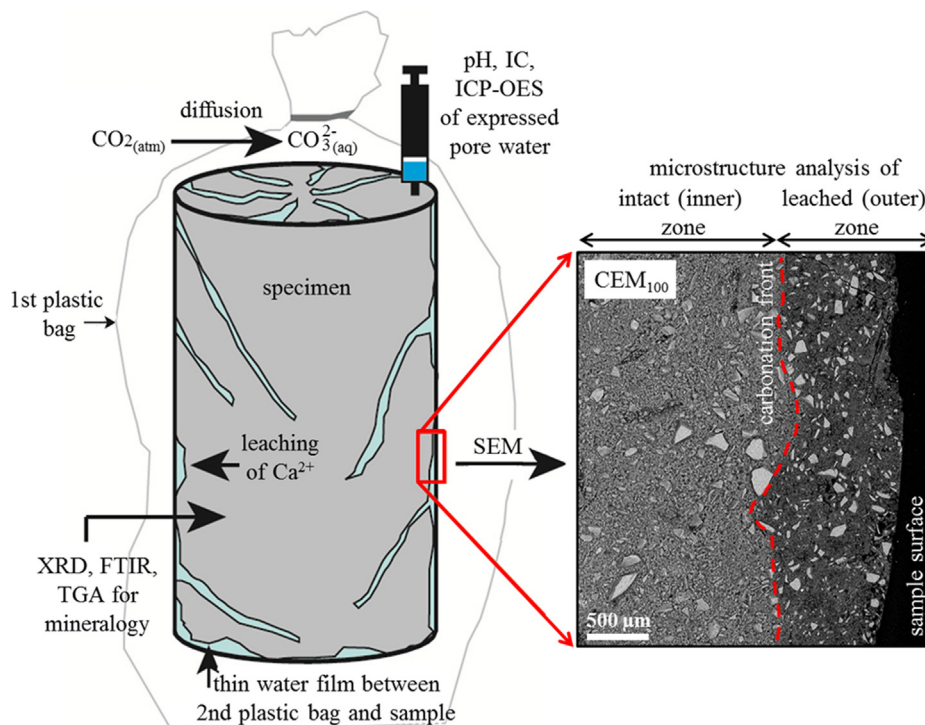


Fig. 1. Schematic representation of the test procedure and multi-methodological approach used in this study.

expressed pore solutions (~1–5 mL) were separated by a syringe and filtered through 0.45 µm cellulose acetate membranes in preparation for subsequent chemical analyses.

For mineralogical and chemical analysis only the samples after 182 days were used and dried in an oven at 80 °C (Bonnet & Balaysac, 2018) for less than 2–3 h in order to avoid thermal alteration and recrystallization of the hydrated cement phases, and then crushed in jaw crusher. Afterwards, the specimens were subjected to visual inspection: all samples showed a modified outer zone and an intact inner zone (Fig. 1), with a thickness of the alteration layer depending mainly on the paste composition. For this reason, three types of sub-samples were considered for the further solid-phase analyses. The first sub-sample having a size of app. 4.5 × 0.7 cm from the surface to the inner zone was prepared for microstructural analyses (see Fig. 1 for leached layer in CEM₁₀₀). The second one was divided into two sub-fractions, namely the altered outer zone and the unaltered inner zone of the specimen, respectively, which were separated by a conventional micro-drill. The latter sub-samples were finely ground in a ball mill for 10 min in preparation for subsequent mineralogical analyses.

2.2. Analytical methods

2.2.1. Solid-phase characterization

The mineralogical composition of the altered and unaltered samples was determined by X-ray diffraction (XRD) of random oriented

powder preparations using a PANalytical X'Pert PRO diffractometer equipped with a Co-radiation source (40 kV, 40 mA), 0.5° antiscattering and divergence slits and a Scientific X'Celerator detector. The preparations were examined in the range from 5 to 50° 2θ range with a step size of 0.004° 2θ and a count time of 40 s per step. Mineral identification was realized with the PANalytical X'Pert HighScore software (version 2.2e) and a pdf-4 database, without consideration of the amorphous phase content [48].

Mid-infrared spectra (MIR) were obtained for further identification of the cement hydrates, as most of these phases are “invisible” by XRD due to their low crystallinity and poorly ordered structure. Therefore, Fourier-transform infrared spectroscopy (FTIR) data was obtained on a PerkinElmer Frontier spectrometer using the attenuated total reflectance (ATR) configuration. The spectra were recorded in the 4000–650 cm⁻¹ range with a point resolution of 2 cm⁻¹.

The proportions of Ca(OH)₂ and CaCO₃ in altered and unaltered pastes were determined by thermogravimetry (TG) and differential scanning calorimetry (DSC) analysis performed on a PerkinElmer STA 8000 thermobalance apparatus. About 30 mg of each sample powder was equilibrated at ~60% relative humidity and then heated from 30 °C to 1000 °C at a constant heating rate of 10 °C/min under N₂ flow. Mineral quantification was realized by evaluation of the TG-curves using the Pyris™ software package and considering the sample-specific weight losses at 450–500 °C for portlandite and at 600–800 °C for carbonates, respectively.

The microstructural characteristics (i.e. microfibrils, total porosity and chemical composition of the cement paste) of the (un)altered parts of each mix were obtained from polished sample surfaces. Observations using backscattered electrons (BSE) were made on a Zeiss Sigma 300 VP scanning electron microscope (SEM) operated at an accelerating voltage of 15 kV. This instrument is equipped with a thermal field emission gun, a solid-state BSE detector and an Oxford Instrument X-max⁸⁰ SDD EDXS (energy dispersive X-ray spectroscopy) detector for elemental analysis, which was used for mineral identification and quantification of the Ca/Si and Al/Si molar ratios of C-S-H. BSE images of 50 μm width and 35 μm height were taken across the (un)altered zones (8–10 for each zone) of each sample to obtain a representative picture of the microstructure. In order to analyze the pore space depicted in these images quantitatively, several image pre-processing steps were applied. Firstly, noise reduction was performed with the non-local means denoising algorithm [49] using the implementation provided by the Avizo software. Secondly, segmentation of the images into pores and solids was made via a global thresholding, i.e. in the resulting binary images the pores and the solids are visualized as black and white regions, respectively. Thirdly, since the interfaces between the two phases were still rough and noisy, binary images were smoothed using morphological closing [50], with a disc of radius 0.04 μm in Matlab. Finally, from these binary images the total porosities of (un)altered zones of each sample were computed, i.e. the areas of all “black objects” in the binary images were summed up and related to the total area of the images to obtain the porosity, that is, the area fraction of pores (see Fig. S1). Median values and median absolute deviations of the porosity for each scenario were calculated (based on 8–10 images per sample) in order to quantify the variability of the porosity. In addition, the area equivalent diameters were computed for every pore cross-section depicted in the image data to characterize the smallest pores: the 1-quantiles (i.e. the value for which 1% of the computed pore diameters are smaller) of pore diameters lie between 27 nm and 100 nm for all considered scenarios, thus making direct comparison of the microstructure of all samples possible.

2.2.2. Fluid-phase characterization

The expressed and filtered pore solutions were analyzed for their pH value and major, minor and trace elemental concentrations. The pH of the pore solutions was measured with a WTW Multi 350i pH-meter equipped with SenTix41 electrode, which was calibrated against NIST buffer standard solutions at pH 7.00 and 10.00. The analytical precision of pH measurements was ± 0.12 pH units at $\text{pH} \geq 13.00$, as determined by replicate analyses of the samples. The chemical composition of the pore solutions was analyzed in replicates with a Dionex ICS-3000 ion chromatograph (IC: Na, K, Ca, SO_4 , Cl) and a PerkinElmer Optima 8300 inductively coupled plasma optical emission spectrometer (ICP-OES: Al, Mg, Si) with an estimated accuracy of $\pm 3\%$ and $\pm 5\%$ for IC and ICP-OES analyses [51], respectively.

For the calculation of the concentrations of OH^- and CO_3^{2-} ions, ion charge balance, aqueous speciation, ionic strength and saturation indices (SI) of the pore solutions with respect to the relevant mineral phases, the PHREEQC software code (version 3.1.5–9133; [52]) in combination with the CEMDATA18 thermodynamic database [53] was used. The following mineral phases were taken into further consideration: portlandite, calcite, C-S-H (i.e. jennite $\text{C}_{1.67}\text{SH}_{2.1}$ -type and tobermorite $\text{C}_{0.83}\text{SH}_{1.3}$ -type), (mono/hemi) carboaluminate, monosulfoaluminate, Si-bearing hydrogarnet (katoite-type), hydrotalcite (i.e. a magnesium aluminium carbonate hydrate that is typically found in slag-blended cements) and ettringite, because of their high relevance (e.g. chemical reactivity) in pure cement paste and hydrated cement blends subjected to leaching and carbonation.

3. Results and discussion

3.1. Pore water geochemistry

The chemical compositions of the pore solutions expressed after 28, 56, 91 and 182 days of reaction time are displayed in Table S1, and important parameters plotted in Fig. 2. It is evident that all pore solutions had a K-Na-OH-type composition, independent from the curing time and original mix design used (Table 1). The OH^- ion concentration and thus the pH of the pore solutions decreased with increasing cement substitution by SCMs, as it can be seen by comparison of CEM₁₀₀ ($\text{pH} \sim 13.5$) with the other hydrated cement blends ($\text{pH} 13.0$ to 13.3). However, the $[\text{Cl}^-]/[\text{OH}^-]$ ratio – a measure for the aggressivity of the pore solutions for corrosion – of CEM₁₀₀ (0.027), CEM₃₀/GS₇₀ (0.030) and CEM₆₀/MEF_{32.5}/MK_{7.5} (0.030) was rather similar. In the case of CEM₉₀/MK₁₀ the ratio of $[\text{Cl}^-]/[\text{OH}^-]$ was lower (0.017), compared to the reference mix. CEM₆₀/MEF_{32.5}/MIF_{7.5} and CEM₉₀/SF₁₀ revealed higher $[\text{Cl}^-]/[\text{OH}^-]$ ratios of 0.047 and 0.103, respectively. Note here that the critical $[\text{Cl}^-]/[\text{OH}^-]$ molar ratio indicated for corrosion risk is 0.6 for a reinforced concrete structures exposed to the atmosphere [54].

This observation matches with findings of Rasheeduzzafar et al. [55], who have shown that the $[\text{Cl}^-]/[\text{OH}^-]$ ratio of hydrated cements blended with 10% and 20% of microsilica can be more than doubled, due to the consumption of OH^- ions during cement hydration. However, based on accelerated corrosion tests (exposure to 5% NaCl solution) these authors have concluded that elevated $[\text{Cl}^-]/[\text{OH}^-]$ ratios in the pore solutions do not negatively affect the start of corrosion (i.e. the initiation time) and hence the material's performance. This may be related to the densification of the cement paste by the pozzolanic reaction between microsilica and $\text{Ca}(\text{OH})_2$ [55]. From these results it can be inferred that the resistance of hydrated cement blends against corrosion cannot be determined by a certain parameter of the pore solution, like the $[\text{Cl}^-]/[\text{OH}^-]$ ratio or a critical threshold Cl^- content, and that other factors of influence, e.g. oxygen availability and aqueous species have to be considered.

Indeed, exposure of pastes to poorly mineralized waters that are undersaturated with respect to dissolved inorganic carbon species represents a leaching scenario (Fig. 1), which is highly relevant for reinforced concrete structures [19]. This is because the boundary conditions used in this test procedure resemble to those often found in tunnels, such as high relative humidity, undersaturation with respect to the CO_2 concentration in air, low to ambient temperature, interaction with soft waters, etc. [22,47]. Specifically, in consequence of CO_2 absorption from the tunnel atmosphere by the alkaline pore solutions developing in concrete, and the subsequent hydroxylation of $\text{CO}_{2(\text{aq})}$ with OH^- ions, both the dissolution of $\text{Ca}(\text{OH})_2$ and the crystallization of anhydrous calcium carbonates, such as calcite, aragonite and vaterite [CaCO_3 polymorphs], are promoted [32].

As expected, the aqueous CO_3^{2-} concentration remained near-constant at 46 ± 6 mg/l for all mixes, suggesting continuous uptake of atmospheric CO_2 into the alkaline pore solutions. Such constant supply of CO_3^{2-} ions is important for the corrosion development of hydrated cement blends, because during carbonation the $\text{Ca}(\text{OH})_2$ content originally present in the paste is progressively consumed in favor of calcite and AFm phase formation. Coincidentally, the pH of the pore solution will start to decrease, from initial pH values of >12 – 13 down to <8 in severely carbonated pastes [19,32,56]. In the present case, the expected drop in pH over time was counterbalanced by the continuous leaching of $\text{Ca}(\text{OH})_2$ and alkali hydroxides (~ 5 – 16 g/l of Na^+ and K^+) from the cement paste, which prevented the samples from severe corrosion. This effect is more

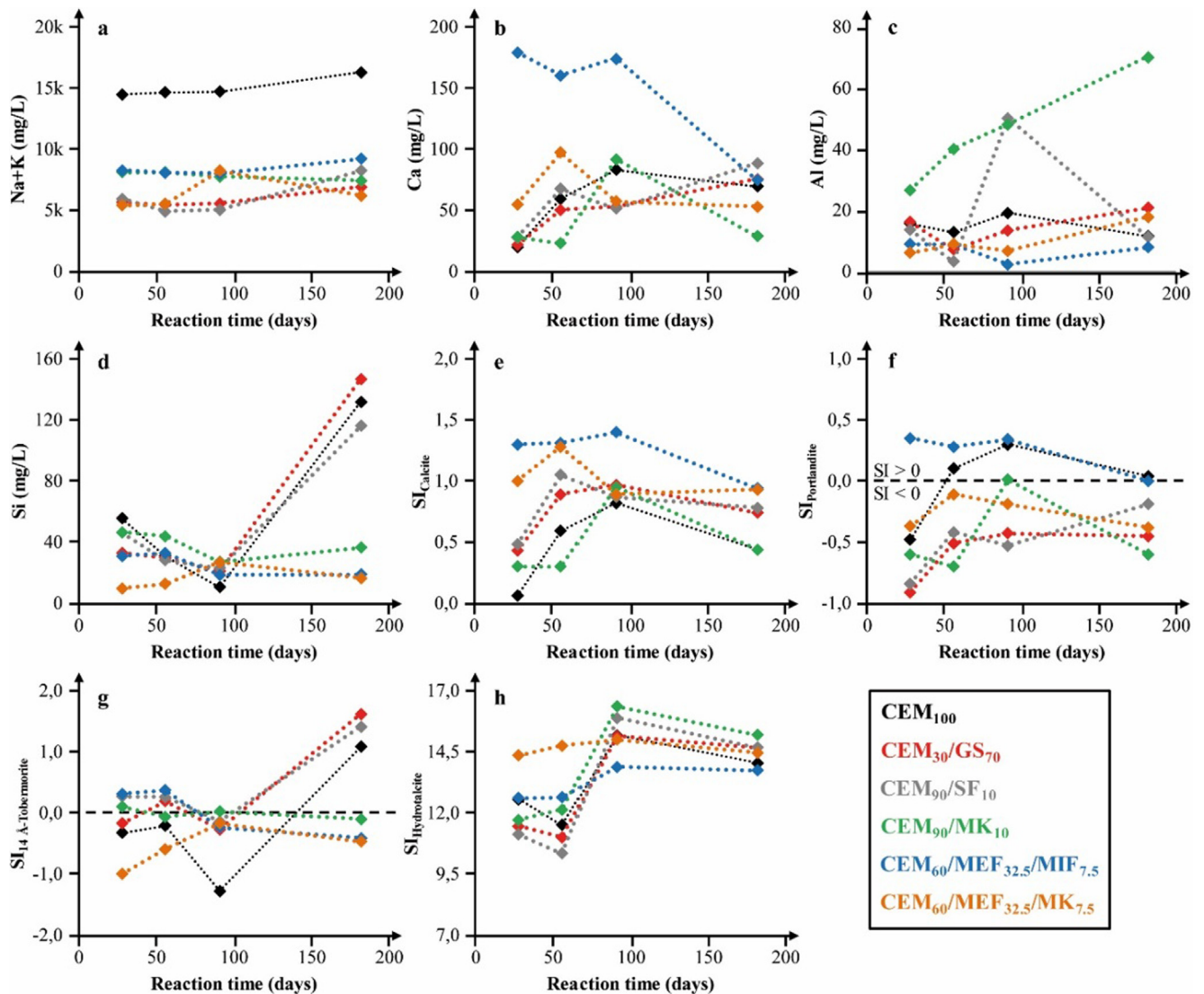


Fig. 2. Temporal evolution of the chemical composition of the pore solutions expressed from cement blends after certain reaction times. Plots are shown for selected elements (K + Na, Ca, Al, Si) and for saturation indices (SI) of portlandite, calcite, tobermorite and hydrotalcite. $SI < 0$ indicates dissolution; $SI > 0$ indicates precipitation.

pronounced in CEM_{100} , which has the highest $Ca(OH)_2$ content among all other samples, as the cements blended with SCMs started consuming some of the $Ca(OH)_2$ already during hydration, in favor of C-S-H formation [22]; thus slightly reducing the system-inherited pH-buffering capacity (Table S1). Besides, elevated concentrations of aqueous Mg^{2+} (1–10 mg/l), Ca^{2+} (20–179 mg/l), Al^{3+} (2–70 mg/l), SO_4^{2-} (28–751 mg/l) and Si^{4+} ions (10–147 mg/l) in the pore solutions of all mix designs suggest (intense) chemical modifications of the cement paste, although the individual element profiles revealed no systematic variations with time (Fig. 2a-d). It is clear that the concentration range of these elements measured in the pore solutions is mainly controlled by the interplay between the dissolving cement clinker phases and subsequently precipitating cement hydrates in each mix.

The results of hydrochemical modelling (Fig. 2 and Table S1) indicate that all pore solutions were close to saturation or slightly undersaturated with respect to portlandite and tobermorite (i.e. SI values < 0 indicate mineral dissolution), but they were dominantly supersaturated with respect to $CaCO_3$ polymorphs, siliceous hydrogarnet (katoite), (mono/hemi)carboaluminate, ettringite, jennite, monosulfoaluminate and hydrotalcite (i.e. SI values > 0 indicate mineral precipitation) after 182 days (Fig. 2f-h). Therefore,

one would expect significant changes in the mineralogical composition and microstructure of the hydrated cement blends after curing in weakly aggressive environment (see sections below for further discussion).

3.2. X-ray diffraction

XRD patterns obtained from unaltered versus altered samples are shown in Fig. 3. The unaltered materials comprised of minor amounts of belite, high amounts of cement hydrates and varying contents of calcite, dolomite and quartz. Portlandite and C-S-H were the most abundant hydration products in all mixes. High amounts of primary calcite were found in the mixes $CEM_{60}/MEF_{32.5}/MIF_{7.5}$ and $CEM_{60}/MEF_{32.5}/MK_{7.5}$, reflecting the mix design (Table 1). The siliceous hydrogarnet group mineral katoite $[Ca_3Al_2(SiO_4)_{0.8}(OH)_{8.8}]$ was more abundant in the samples CEM_{90}/MK_{10} and $CEM_{60}/MEF_{32.5}/MK_{7.5}$, due to additional supply of reactive silica from the MK additives [57–59]. The mix CEM_{30}/GS_{70} developed by far the highest contents of hydrotalcite $[Mg_6Al_2CO_3(OH)_{16} \cdot 4(H_2O)]$ and of other AFm phases, which is typical for cement blended with slag [60]. The presence of Friedel's salt cannot be excluded in these mixes, as its main reflection

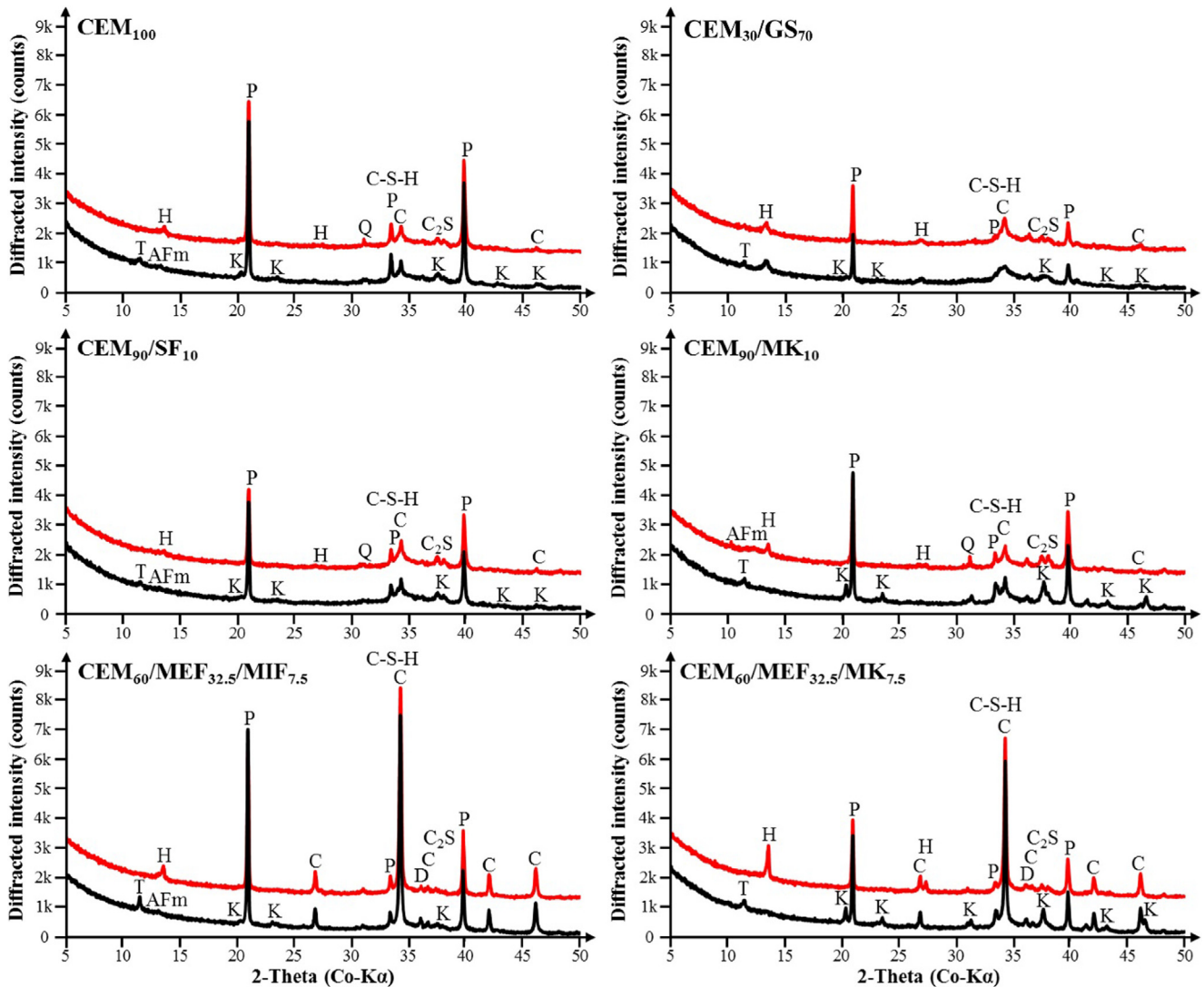


Fig. 3. XRD patterns of hydrated cement blends after curing for 182 days (black and red curves correspond to unaltered and altered samples, see Fig. 1). T – 9 Å-tobermorite, AFm – calcium aluminate hydrate, H – hydrotalcite, P – portlandite, K – katoite, C – calcite, C-S-H – calcium silicate hydrate, D – dolomite, C₂S – belite.

overlaps with the peaks of other AFm phases, and since this phase is known to form solid solutions with some AFm phases [20]. Similarly, vaterite could be barely present in all mixes, though its main reflections (011 and 012) are poorly developed and partly overlap with those of belite (202̄ and 022̄). The presence of 9 Å-tobermorite in the unaltered samples results from drying at 80 °C, rather than indicating incomplete cement hydration, as 14 Å-tobermorite [Ca₅Si₆O₁₆(OH)₂·7H₂O] forms during wet storage [61–63].

In contrast, katoite and tobermorite were absent in the altered samples, and the portlandite peaks significantly lost intensity (Fig. 3), which suggests dissolution of these mineral phases. The reflections of calcite (±vaterite) and hydrotalcite have gained intensity, which points to the accumulation of these phases in the altered zone, confirming the hydrochemical modelling results (Table S1). However, it is worthy to note that portlandite, tobermorite, hydrotalcite and katoite among others are quantitatively consumed during carbonation. This indicates that the carbonation reaction has not been fully completed after 182 days of reaction time [59], probably reflecting the “mild” exposure conditions used in this research. Also, the neo-formation of ettringite was not observed in all mixes, despite of potentially favorable formation conditions (Table S1).

Similar alteration patterns have been observed in cements blended with alkali activated blast-furnace slag pastes, i.e. tobermorite and katoite progressively transformed into hydrotalcite, thereby inducing microstructural damage to the cement matrix [64–66]. Bernal et al. [59] have proposed that the rate of this reaction strongly depends on the CO₂ concentration, as it directly affects the pH of the pore solutions and related alkali carbonate/bicarbonate phase equilibria. Given the relatively low CO₂ concentration in air (~400 ppm), the carbonation reactions mentioned before should be slow, compared to accelerated systems applying app. 2 to 4% of CO₂, but similar to those observed in tunnel environments [22]. Future research is needed to constrain the relations between mineral phase reactivity, alteration mineralogy and corrosion behavior of hydrated cement blends exposed to CO₂ environments.

3.3. Infra-red spectroscopy

MIR spectra of samples taken from the unaltered versus altered zone of the test specimens are shown in Fig. 4. The presence of portlandite in all sample types is indicated by an IR band at 3643 cm⁻¹. Very broad and weak double peaks at ~1000 cm⁻¹

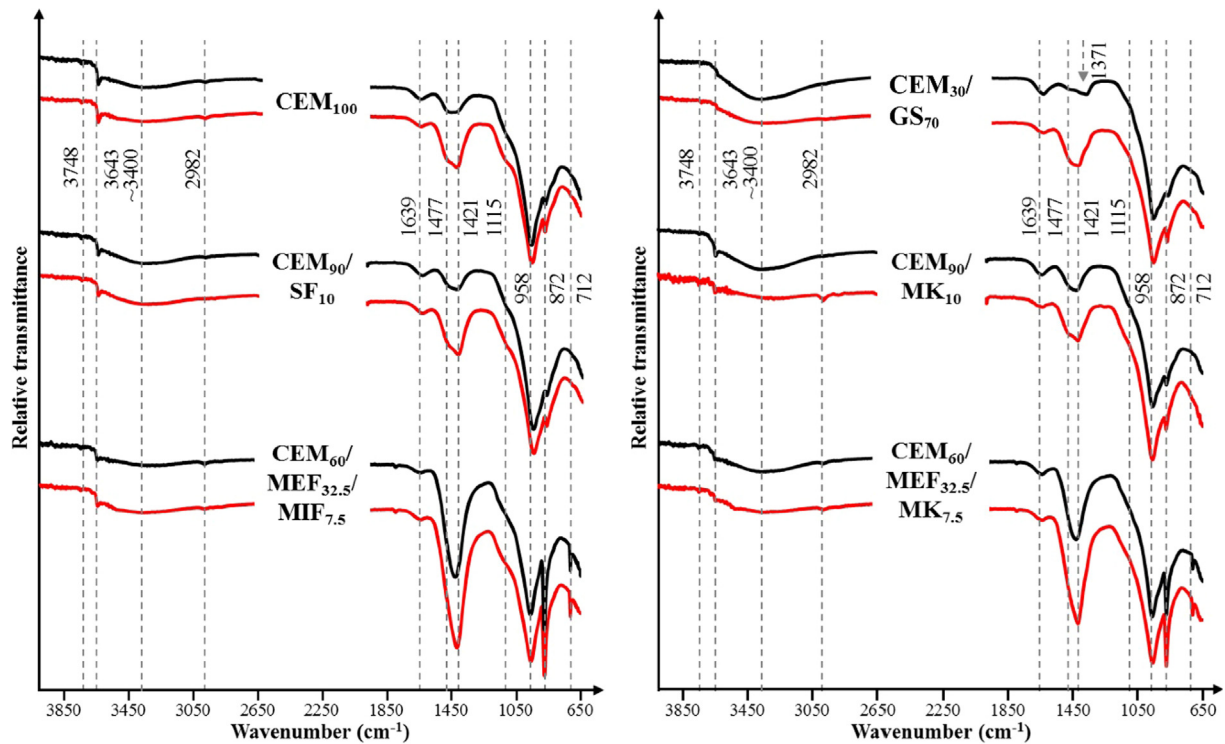


Fig. 4. FTIR patterns of hydrated cement blends after hardening in plastic bags for 182 days (black and red curves correspond to unaltered and altered samples, see Fig. 1). (For interpretation of the references to colour in this figure legend, the reader is referred to the web version of this article.)

and $\sim 900\text{ cm}^{-1}$ (Si-O asymmetric stretching vibrations) correspond to traces of belite [67,68]. Adsorption at 872 cm^{-1} and 712 cm^{-1} (asymmetrical/symmetrical deformation vibrations of CO_3^{2-}) is related to occurrences of calcite in all samples. The relative increase in intensity of the 1421 versus 1477 cm^{-1} band (asymmetrical stretching of CO_3^{2-}) in the altered samples suggests a shift towards decreasing particle sizes and surface roughness of secondary calcite and vaterite that form due to CO_2 ingress through the plastic bag wall [56,69]. The adsorption centered at $\sim 3400\text{ cm}^{-1}$ and 1639 cm^{-1} is related to OH^- stretching modes and H-O-H bending modes in various hydroxyl groups and in surface-bound water [70]. The weak adsorption at 2982 cm^{-1} is due to the presence of trace amounts of ethanol remaining in the solids from preparation (C-H stretching vibration, [16]). The IR band at 1371 cm^{-1} (asymmetrical stretching of CO_3^{2-}) is assigned to hydrotalcite and AFm phases in all samples [71]. This IR band is more pronounced in $\text{CEM}_{30}/\text{GS}_{70}$ due to high amounts of hydrotalcite in this mix (Fig. 3). Adsorption at 3748 cm^{-1} , 1115 cm^{-1} and in the range between 1200 and 800 cm^{-1} refers to Si-O-Si and Si-O-Al stretching vibrations in tobermorite, katoite and poorly crystallized C-S-H [72,73].

The main adsorption shifted from $\sim 960\text{ cm}^{-1}$ to $\sim 950\text{ cm}^{-1}$ for C-S-H from the unaltered and altered zone of each sample, independent for the original mix design used. This systematic decrease towards lower wavenumbers suggests intense modifications of the C-S-H structure due to progressive calcium leaching and related recrystallization. Such alteration patterns are typically associated with (i) decreasing polymerization of the tetrahedral chains of C-S-H, (ii) substitution of Si-O-Si by Si-O-Al bonds and (iii) lowering of the Ca/Si ratio in the C-S-H structure [74]. These processes are further seen by an increase in intensity of the $\sim 1100\text{ cm}^{-1}$ band of C-S-H in the altered zone, which is assigned to abundant structural defects (Fig. 4). In terms of corrosion, calcium-depleted and highly defect (tobermorite-type) C-S-H should have a higher solubility than the calcium-rich (jennite-type) counterparts [75], thus affecting the chemical reactivity of the paste.

3.4. Thermogravimetric analysis (TGA)

The TG- and DSC-curves of samples taken from the altered versus unaltered zones of the hydrated cement blends and reference mix exhibited a strong weight loss (-5.0 to $-12.9\text{ wt}\%$) between 30°C and 200°C (i.e. the main peak was located at ~ 130 – 140°C) and a second moderate one between 450°C and 500°C (-1.4 to $-5.7\text{ wt}\%$). Another relatively weak weight loss was observed between 600°C and 670°C (-1.1 to $-3.8\text{ wt}\%$) and a fourth weak to strong one (-0.3 to $-14.4\text{ wt}\%$) between 670°C and 800°C . The DSC-signal revealed in all cases negative excursions, which is indicative of endothermic reactions. Hence, these weight losses have been attributed to the removal of H_2O and CO_2 molecules from C-S-H and AFm phases ($<200^\circ\text{C}$), dehydroxylation of portlandite ($\sim 480^\circ\text{C}$) and decomposition of vaterite ($<670^\circ\text{C}$) and calcite (670 – 800°C), respectively [76]. Accordingly, the weight losses obtained in these temperature ranges are tabularized in Table 2, together with changes in the $\text{Ca}(\text{OH})_2$ and CaCO_3 contents upon leaching and carbonation, for all samples. It should be noted that we cannot report absolute contents for C-S-H, because of formation of multi-phase products (tobermorite, hydrotalcite and AFm, katoite etc.) and potential modifications of the water content of tobermorite induced during sample curing and drying (i.e. presence of 9 \AA - tobermorite instead of 14 \AA -tobermorite).

The portlandite content was reduced and the C-S-H phase content was increased in hydrated cements substituted with GS, SF and MK, compared to CEM_{100} , due to consumption of $\text{Ca}(\text{OH})_2$ during hydration of SCMs [25,28]. However, the CaCO_3 content in these mixes was relatively similar (1.4 to $2.5\text{ wt}\%$). $\text{CEM}_{60}/\text{MEF}_{32.5}/\text{MIF}_{7.5}$ and $\text{CEM}_{60}/\text{MEF}_{32.5}/\text{MK}_{7.5}$ displayed much lower C-S-H and $\text{Ca}(\text{OH})_2$ contents, but a high CaCO_3 content, which reflects the high level of limestone substitution for cement in these mixes (Table 1) and the low reactivity of carbonate fillers during cement hydration [12,77].

A reduction in the volatile content of C-S-H (Table 2), a strong loss in the portlandite content (Fig. 5a) and a sudden increase in

Table 2

Compilation of weight losses of C-S-H, portlandite (P), vaterite (V) and calcite (C) within the hydrated cement blends as a function of mix design approach (unaltered zones) and exposure to calcium leaching and carbonation (altered zone), based on TGA data. Variations in the quantitative phase contents of portlandite and secondary calcium carbonates (Carb) are given as Δ -values (calculated by the difference of mineral abundances in the unaltered and altered zones). Note the imbalance in the calcium budget between reaction educts and products for all samples (Fig. 5d). See text for further explanations.

Sample ID	Position of sample	C-S-H [†] wt-%	P wt-%	V wt-%	C wt-%	Δ -P wt-%	Δ -Carb wt-%
CEM ₁₀₀	unaltered zone	8.1	5.7	1.3	0.8		
CEM ₁₀₀	altered zone	7.7	4.5	1.7	3.8	-5.1	6.7
CEM ₃₀ /GS ₇₀	unaltered zone	12.9	1.4	1.1	0.3		
CEM ₃₀ /GS ₇₀	altered zone	6.8	1.5	2.1	1.7	0.2	3.1
CEM ₉₀ /SF ₁₀	unaltered zone	12.0	3.6	1.2	0.8		
CEM ₉₀ /SF ₁₀	altered zone	8.6	3.3	1.9	2.3	-1.4	3.3
CEM ₉₀ /MK ₁₀	unaltered zone	12.2	3.4	1.6	0.8		
CEM ₉₀ /MK ₁₀	altered zone	9.1	3.1	3.0	0.6	-1.1	-0.4
CEM ₆₀ /MEF _{32.5} /MIF _{7.5}	unaltered zone	5.0	3.8	2.8	13.9		
CEM ₆₀ /MEF _{32.5} /MIF _{7.5}	altered zone	5.2	3.5	3.5	14.4	-1.2	1.0
CEM ₆₀ /MEF _{32.5} /MK _{7.5}	unaltered zone	8.4	2.1	2.5	11.7		
CEM ₆₀ /MEF _{32.5} /MK _{7.5}	altered zone	7.5	1.9	3.8	11.5	-0.6	-0.5

[†] Refers to the volatile content of all hydrated cement phases (i.e. weight loss in the temperature range from 30 °C to 200 °C)

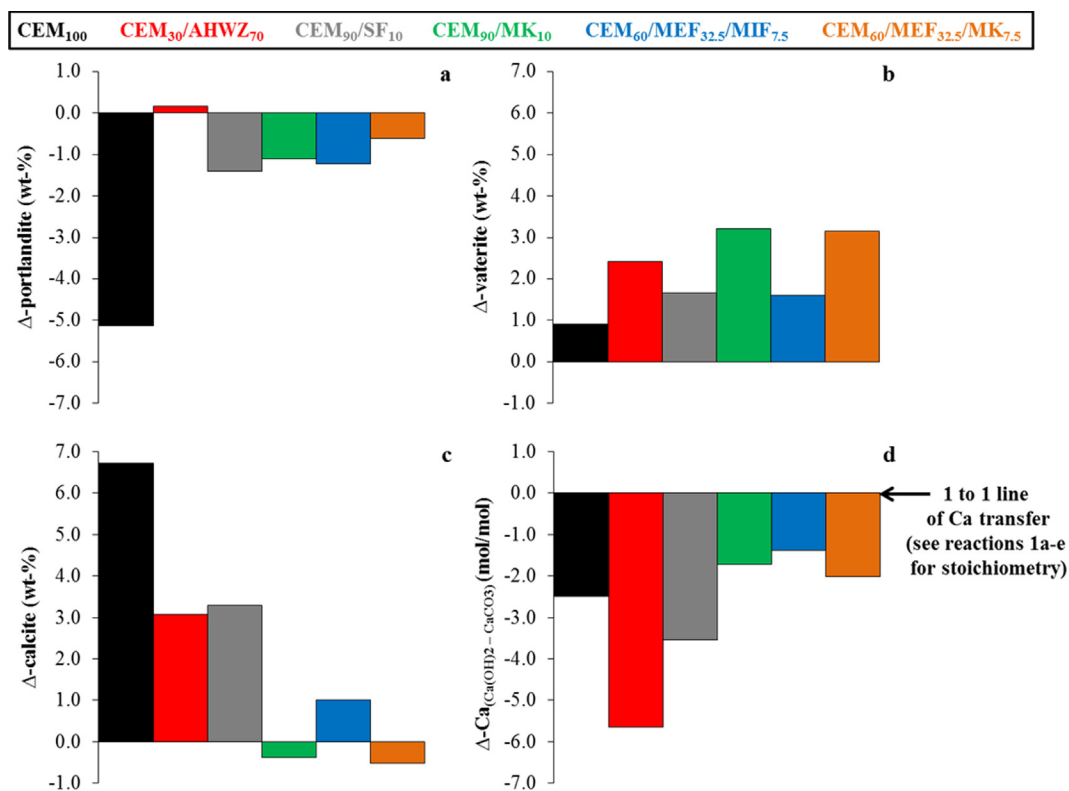


Fig. 5. Change in the portlandite (a), vaterite (b) and calcite (c) content of hydrated cement blends after curing in weakly aggressive environments. Negative values indicate mineral dissolution; positive values indicate mineral neo-formation. Note the imbalance in the calcium budget between the ideal dissolution portlandite and formation of calcite + vaterite (reported as Δ -Ca ratio in d, where the stoichiometric reaction is indicated by the 1 to 1 line), which is counterbalanced by calcium leaching from C-S-H.

the amounts of neo-formed vaterite (Fig. 5b) and calcite (Fig. 5c) were evident by comparison of samples collected from the altered and unaltered zone of each mix. CEM₁₀₀ showed by far the highest decrease in the portlandite content and the highest increase in the carbonate content, compared to the hydrated cement blends (Table 2), which suggests an outstanding performance of the blends in terms of protection of reinforcement (see section on microstructure for further evaluation).

Importantly, stoichiometric considerations of the calcium budget (defined as Δ -Ca) yielded an imbalance for all mixes: there is much more calcium associated with the secondary carbonates than it could have been theoretically provided by the dissolution of portlandite (i.e. all values plot below the 1:1 line for Δ -Ca in Fig. 5d). For example, in CEM₁₀₀ one can see a loss of -5.1 wt-%

of portlandite and a gain of +7.6 wt-% of calcite, which is equivalent to a Δ -Ca excess of ~39% in the alteration zone (Table 2). This finding documents the reactivity of hydrated cement phases even under highly alkaline conditions (pH \geq 13.0, Table S1), i.e. it is suggested that leaching of tobermorite, katoite, etc. provided an important fraction of Ca²⁺ ions to the pore solutions to be used for the subsequent formation of CaCO₃ polymorphs.

3.5. Microstructure analysis (SEM)

3.5.1. Evaluation of alteration patterns

Alteration features within CEM₁₀₀ are displayed in Fig. 6. From the BSE image sequences (Fig. 6a-f) and EDX spectra of C-S-H collected from the unaltered and altered zones (Fig. 6g) one can see

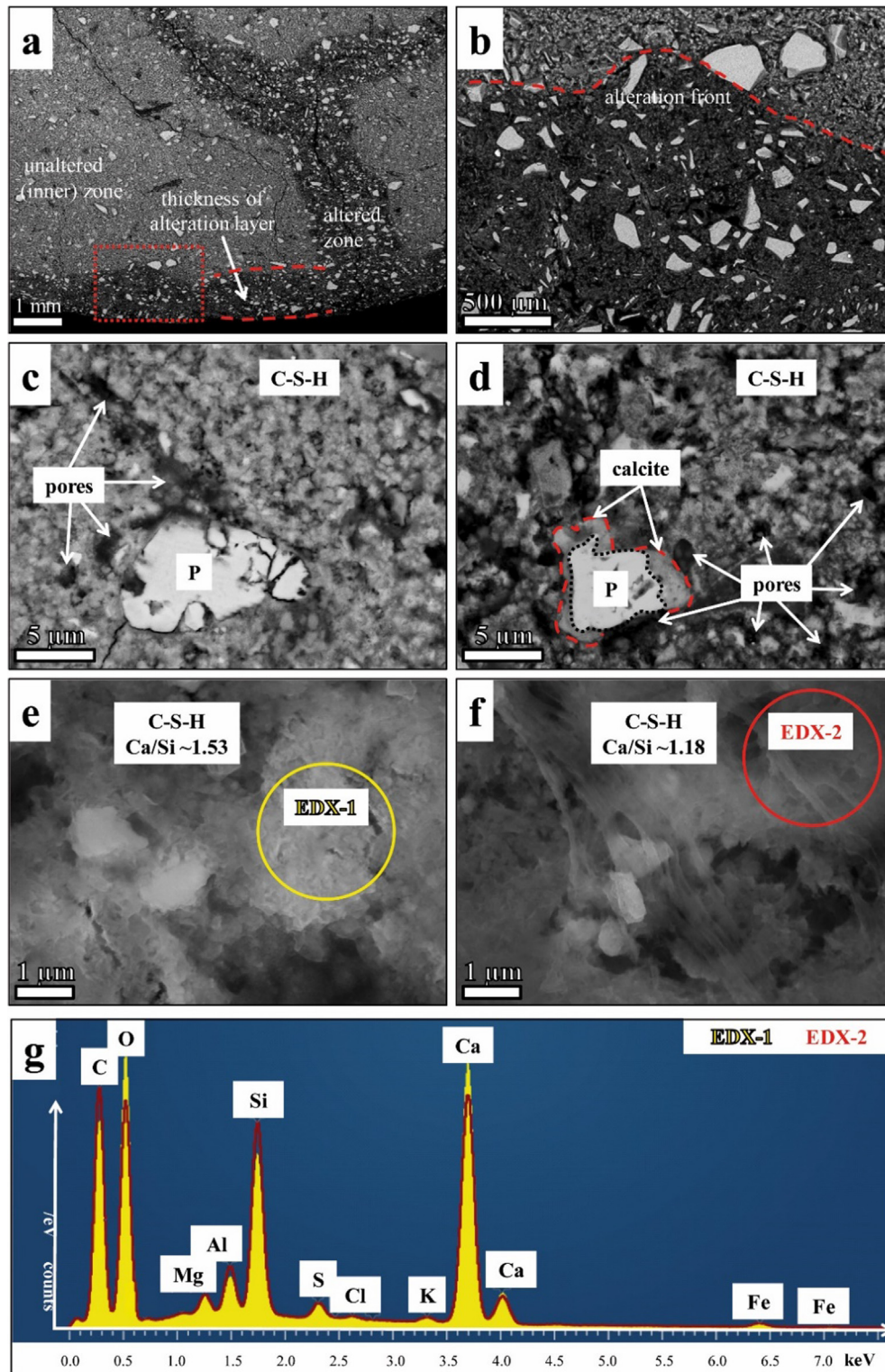


Fig. 6. (a) BSE image showing the transition zone between altered (dark grey areas with porous microfabrics) and unaltered parts (light grey areas with denser microfabrics) of CEM₁₀₀. (b) Close-up of (a) marked with red rectangle. Note the increase in porosity due to curing in weakly aggressive environments. (c,d) Close-ups showing portlandite grains with/without thin calcite layers. (e,f) High-resolution BSE images displaying changes in the particle form and Ca/Si molar ratio of C-S-H due to Ca-leaching and recrystallization (e: inner zone; f: outer zone). (g) Normalized EDX spectra of C-S-H from the unaltered (EDX-1) versus altered (EDX-2) zone (spot positions are marked in e,f). P – portlandite. (For interpretation of the references to colour in this figure legend, the reader is referred to the web version of this article.)

significant microstructural, mineralogical and geochemical modifications of the cement paste due to leaching, which are described in detail below (note that all other samples blended with SCMs were evaluated in this way).

The corrosive layer of CEM₁₀₀ had a thickness of $1470 \pm 220 \mu\text{m}$, as it is indicated by 30 replicate measurements across the entire sample surface (Fig. 6a). The boundary between the unaltered and altered zone is marked by an extremely thin transition zone

(e.g. the interfacial transition zone is less than 100 nm thick in Fig. 6a-b), reflecting the onset of leaching and carbonation [15,19,20]. In the inner parts of CEM₁₀₀, portlandite and more rarely belite occurred as isolated grains within the very dense C-S-H matrix (total porosity: $9.5 \pm 2.0\%$, Fig. 6c). In the outer parts, belite and portlandite were leached away or were passivated by a thin calcite layer (Fig. 6d and reaction 1), which prevented these phases from further dissolution [22].

A strong increase in the total porosity to about $23.1 \pm 7.0\%$ was evident in the altered zone of CEM₁₀₀, which is related to (i) dissolution of cement clinker phases and portlandite (Fig. 6d), (ii) alteration of tobermorite, AFm phases and katoite into hydrotalcite (Fig. 3) and (iii) calcium leaching and recrystallization of C-S-H (Fig. 4). The latter is seen by a decrease in the Ca/Si molar ratio, from 1.71 ± 0.20 to 1.23 ± 0.21 , and an increase in the Al/Si molar ratio, from 0.12 ± 0.05 to 0.24 ± 0.09 , of C-S-H from the unaltered versus altered zones (Fig. 6g). The SEM-EDX data further revealed a very low Na content (≤ 0.2 wt-%) and a low Mg content (0.5–1.3 wt-%) of C-S-H from CEM₁₀₀, which implies that sodium aluminosilicate hydrates (N-A-S-H) and magnesium aluminosilicate hydrates (M-A-S-H) did not form to a great extent in this mix [78,79].

3.5.2. Thickness of leached layer

The alteration front that developed around all types of hydrated cement blends was ~ 3.5 up to ~ 12.3 times smaller compared to CEM₁₀₀ after 182 days of reaction time (Table 3). In detail, CEM₃₀/GS₇₀, CEM₉₀/SF₁₀ and CEM₆₀/MEF_{32.5}/MK_{7.5} displayed the smallest thicknesses of the altered layer (< 0.2 mm), suggesting an outstanding resistance of these mixes against calcium leaching and carbonation, judged by direct comparison with CEM₁₀₀. CEM₉₀/MK₁₀ and CEM₆₀/MEF_{32.5}/MIF_{7.5} revealed alteration thicknesses of circa 0.4 mm, which justifies the excellent performance of these mixes. Noteworthy, the alteration patterns observed were not restricted immediately to the sample surface, as dissolution veins progressed into the deeper parts (up to a few millimeters, Fig. 6a) of CEM₁₀₀ (and CEM₆₀/MEF_{32.5}/MK_{7.5}). We therefore conclude that exposure of cementitious materials to low-mineralized solutions undersaturated with respect to the atmospheric CO₂ concentration can cause deterioration of the cement paste within short times. This leaching process reduces the resistivity of steel-reinforced concrete to carbonation, especially when subjected to wetting–drying cycles and under permanent exposure to air.

3.5.3. Microfabrics, C-S-H composition and porosity development

Important microstructural data of the hydrated cement blends are provided in Table 3 for the unaltered and altered zones of each sample. Corresponding BSE images are presented in Figs. 7 and 8.

Note that all images have been collected at the same magnification and brightness/contrast to ensure direct comparison between the samples.

In the unaltered zone, all cement pastes are dense, as indicated by total porosities from $5.7 \pm 2.0\%$ to $9.5 \pm 2.0\%$ (Table 3). The substitution of CEM 1 by SCMs decreased the portion of clinker in the mixes and hence the water/clinker ratio (e.g. 40% in CEM₆₀/MEF_{32.5}/MIF_{7.5}). Nevertheless, the porosity in the unaltered zone was lower for all blended cements than for CEM₁₀₀, up to 30%. This is because of an increase in the total volume of the reaction products that form in the cement blends upon cement hydration plus latent-hydraulic or pozzolanic reaction, compared to CEM₁₀₀. Indeed, the hydration of the cement blends with hydraulically active SCMs benefited from prolonged curing (182 days) at high water content (as defined by the w/b-ratio) and humidity. Regarding blends with inert limestone powders (CEM₆₀/MEF_{32.5}/MIF_{7.5} and CEM₆₀/MEF_{32.5}/MK_{7.5}), the increased packing density due to a microfiller effect [11,77] caused low porosity despite high water/clinker-ratios. All effects have resulted in a densification of the microstructure of the hydrated cement blends, as it is seen in the development of more fine pores and less coarse capillary pores than in CEM₁₀₀ (Fig. 8c). This effect is particularly relevant for mixes containing MIF/MEF limestones.

C-S-H had a very fine or cloudy (Fig. 7a,e and 8a,c,e) to foil-like particle form (Fig. 7c). As expected, the chemical composition of C-S-H changed as a function of type and level of cement replacement by SCMs (Table 3), confirming predicted trends within the CaO–Al₂O₃–SiO₂ ternary diagram of cementitious materials [12]. This is seen by shifts in the molar ratios of Ca/Si (1.71 ± 0.20 to 1.39 ± 0.33) and Al/Si (0.12 ± 0.05 to 0.37 ± 0.04) for CEM₁₀₀ and CEM₃₀/GS₇₀, respectively. M-A-S-H eventually formed in hydrated cements blended with GS, MK, MEF and MIF, taking the high MgO contents (up to 3.5 wt-%) in the unaltered samples and high hydrotalcite contents in the reacted samples (Fig. 3).

The microstructure seen within the altered zone was completely different, compared to the unaltered zone (Table 3). For example, the microfabric was generally more porous (see Fig. 7b,f and 8f), as it is seen by a doubling in the total porosity of CEM₁₀₀ and a moderate (~ 5 – 10%) to high ($\sim 30\%$) increase in the total porosities of all the other mixes, due both to portlandite dissolution and recrystallization of C-S-H. Abundant micro-cracks of variable thickness and length have been developed in this altered zone (see Fig. 6a for CEM₁₀₀). The portlandite crystals, remaining after leaching, displayed a thin calcite layer (Fig. 7b,d and 8b,d) that prevented this phase from complete dissolution [22].

Microstructural modifications within the altered zones further included changes in the form of C-S-H particles (Table 3), altering

Table 3

Compilation of microstructural data for the unaltered and altered zones of hydrated cement blends (see Figs. 6–8 for direct comparison of microfabrics, porosity and C-S-H composition) after 182 days of curing. Note the larger thickness of the corrosive layer and the increase in porosity in CEM₁₀₀, compared to all other cement blends, as well as the decrease in the Ca/Si ratio and the increase in the Al/Si molar toward the corrosion zone.

Sample ID	Thickness of corrosive layer (μm)	Sample description	Porosity (%)	Number of BSE images analyzed	Microfabric of C-S-H	Ca/Si ratio of C-S-H (molar)	Al/Si ratio of C-S-H (molar)	Number of EDX analyses
CEM ₁₀₀	1470 ± 220	unaltered	9.5 ± 2%	10	fine, dense	1.71 ± 0.20	0.12 ± 0.05	5
CEM ₁₀₀		altered	23.2 ± 7%	10	fibrillar, weak	1.23 ± 0.21	0.24 ± 0.09	6
CEM ₃₀ /GS ₇₀	120 ± 40	unaltered	5.7 ± 2%	9	foil-like, dense	1.39 ± 0.33	0.37 ± 0.04	6
CEM ₃₀ /GS ₇₀		altered	6.2 ± 1%	9	foil-like, dense	1.16 ± 0.27	0.32 ± 0.06	4
CEM ₉₀ /SF ₁₀	170 ± 50	unaltered	6.9 ± 2%	10	fine, dense	1.57 ± 0.14	0.14 ± 0.07	3
CEM ₉₀ /SF ₁₀		altered	9.8 ± 2%	8	fibrillar, weak	1.21 ± 0.09	0.25 ± 0.08	6
CEM ₉₀ /MK ₁₀	370 ± 80	unaltered	6.4 ± 1%	8	fine, dense	1.59 ± 0.22	0.31 ± 0.05	3
CEM ₉₀ /MK ₁₀		altered	5.6 ± 12%	10	foil-like, dense	1.32 ± 0.17	0.35 ± 0.06	5
CEM ₆₀ /MEF _{32.5} /MIF _{7.5}	420 ± 60	unaltered	7.3 ± 2%	8	fine, dense	1.53 ± 0.25	0.16 ± 0.04	4
CEM ₆₀ /MEF _{32.5} /MIF _{7.5}		altered	8.0 ± 5%	8	fine, dense	1.34 ± 0.11	0.23 ± 0.08	6
CEM ₆₀ /MEF _{32.5} /MK _{7.5}	210 ± 40	unaltered	6.2 ± 2%	8	fine, dense	1.56 ± 0.19	0.27 ± 0.11	3
CEM ₆₀ /MEF _{32.5} /MK _{7.5}		altered	6.2 ± 3%	8	foil-like, dense	1.32 ± 0.16	0.30 ± 0.07	5

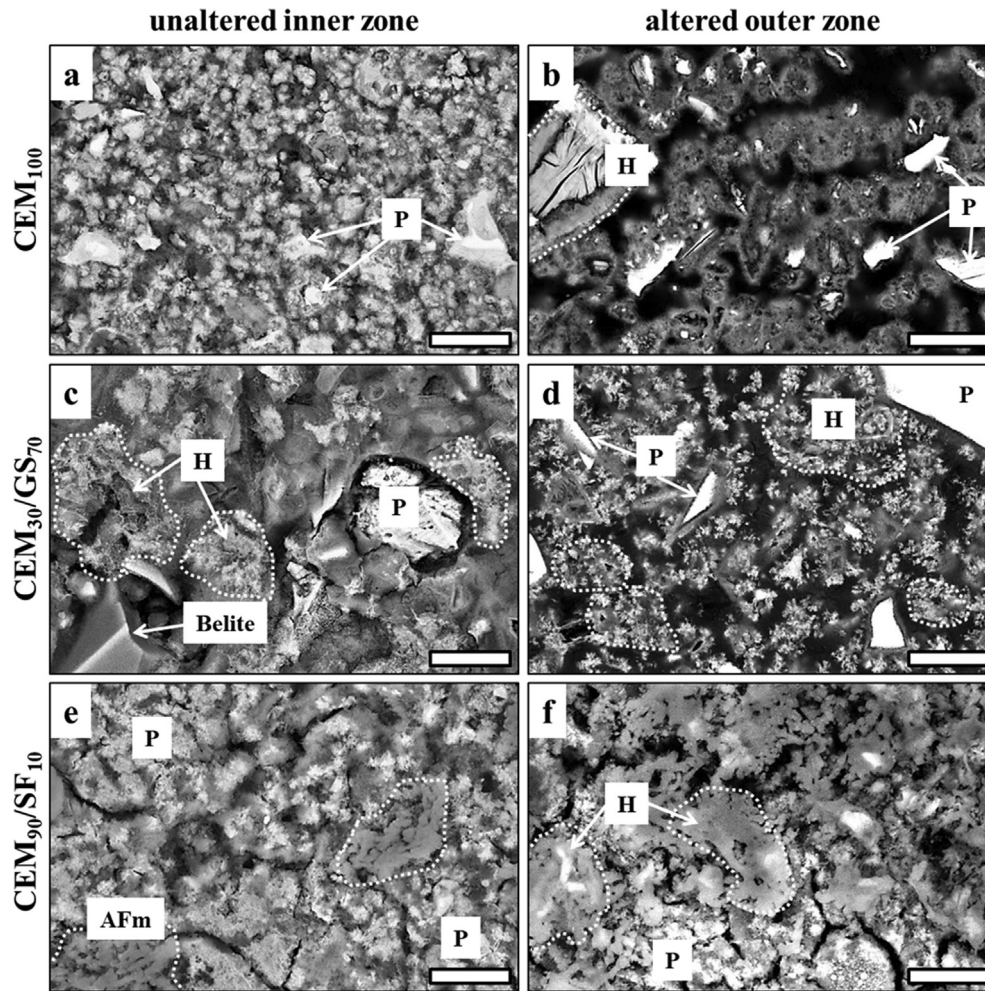


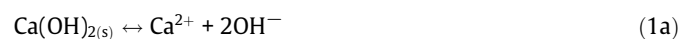
Fig. 7. BSE images showing the effect of SCM substitution for cement on the microfabrics of hydrated cement blends and hydrated reference cement (i.e. inner zone) as well as alteration features associated with combined calcium leaching and carbonation (i.e. altered outer zone). Microfabrics are denser and portlandite crystals are smaller in hydrated cement blends, suggesting consumption of $\text{Ca}(\text{OH})_2$ during hydration of SCMs. Note the increase in porosity (especially in CEM_{100}), the formation of patches of hydrotalcite and the decrease in brightness (i.e. reflecting a higher degree of calcium leaching from C–H, see Table 3) in the altered samples. AFm – calcium aluminate hydrate, H – hydrotalcite, P – portlandite. Scale bar: 10 μm .

from very fine and dense frameworks to fibrillary, foil-like and generally weaker ones (compare Fig. 7a,b and 8e,f). Moreover, recrystallized C–S–H had a lower Ca/Si molar ratio and a higher Al/Si molar ratio than the unaltered C–S–H (Table 3) due to leaching [16]. Taking this all together, significant deterioration of the microstructure of CEM_{100} relative to hydrated cement blends occurred over the course of leaching and carbonation, which expresses in a chemical weakening of the cement matrix and lack of cohesion between the cement paste and particles.

3.6. Comparison of leaching behavior of hydrated cement blends

The results of mineralogical, microstructural and geochemical changes of the hydrated cement blends due to leaching and carbonation attack can be summarized as follows: (i) a leached layer and pervasive cracks of variable thickness and length developed around the specimen's surface, (ii) portlandite transformed into calcite (\pm vaterite) and very often a thin passivation layer of calcite formed around the portlandite crystals, (iii) tobermorite and katoite (\pm AFm phases) altered into hydrotalcite, (iv) the Ca/Si molar ratio of C–S–H decreased, while the Al/Si molar ratio increased within the alteration zone, and (v) the total porosity increased towards the active leaching and carbonation front.

Judging from these criteria, CEM_{100} performed worse than the hydrated cement blends, since the reference mix exhibited the highest total porosity (Figs. 7 and 8), the highest portlandite loss (Fig. 5) and the highest decrease in the Ca/Si molar ratio of C–S–H (Fig. 6g and Table 3) among all the other samples under evaluation. This indicates that the decalcification process in OPC paste is generally faster than in the hydrated cement blends (Table 1). This is contrary to the results reported in Słomka-Słupik et al. [20], who have argued that slag-blended materials degrade faster than CEM I during ammonium chloride attack, which they attributed to the presence of micro-cracks along the slag grains and the high self-healing capacity of OPC pastes. Such a self-healing effect, i.e. precipitation of secondary portlandite, was not observed in this study, because the pore solutions were predominantly undersaturated with respect to this mineral phase at any time of reaction (see Fig. 2f and Table S1). Consequently, portlandite was consumed in favor of calcite precipitation, following reaction (1a)–(1e):



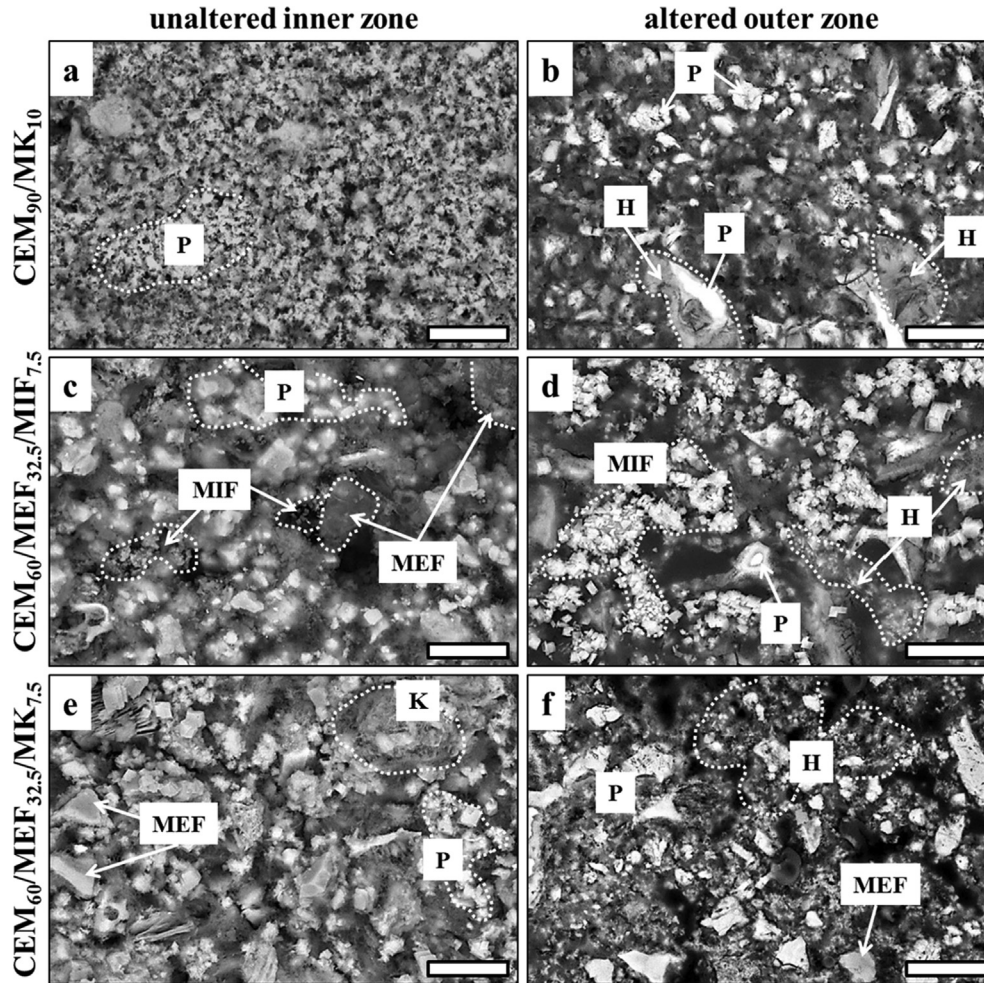
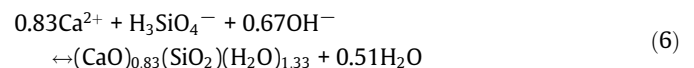
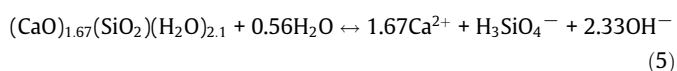
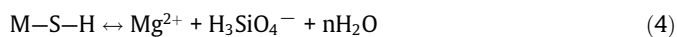
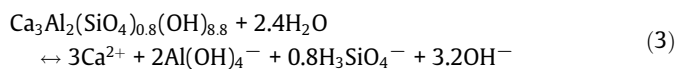
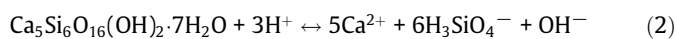


Fig. 8. Continuation of Fig. 7 showing the effect of SCM substitution for cement on the microfabrics of hydrated cement blends as well as alteration features due to curing in weakly aggressive environments. H – hydrotalcite, K – katoite, MEF – limestone mesofiller, MIF – limestone microfiller, P – portlandite. Scale bar: 10 μm .



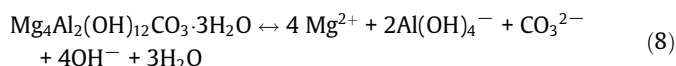
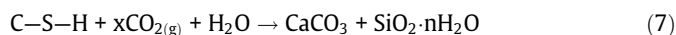
Ruiz-Agudo et al. [80] have proposed that no secondary porosity is generated during the carbonation of portlandite. The data obtained in this study do not support this viewpoint, as it can be inferred from the formation of micro-cracks, the increase in secondary porosity and the expansion of the leaching front in CEM₁₀₀ (Fig. 6a–d), i.e. the mix with the highest portlandite loss. Progressive calcium leaching from the cement paste is evident by the disappearance of tobermorite and katoite in the alteration zone (Figs. 3 and 4), and by the alteration of jennite-type C-S-H to tobermorite-type C-S-H (Fig. 6 and Table 3), following to Eqs. (2)–(6):



It is clear that these dissolution processes (Eqs. (3)–(6)) will produce secondary pore space within the cement paste. Calcium leaching from C-S-H and subsequent alteration into a Ca-depleted form (Eq. (7)) is well-known to affect the mechanical properties (i.e. reduction of strength) and solubility (expressed by the logarithm of the solubility constant for a certain mineral, $\log K_{sp}$) of the hardened cement paste [81]. In this line, Walker et al. [75] have reported on an increase in the $\log K_{sp}$ values, from -13.08 to -10.33 , for C-S-H having Ca/Si molar ratios of 1.65 and 1.15, respectively, which is similar to the compositions determined in this study (Table 3). In other words, this shift in the Ca/Si composition is equivalent to an increase of nearly three orders of magnitude in solubility constants for the two forms of C-S-H.

We therefore suggest that dissolution and recrystallization phenomena within the cement paste greatly affect the life performance of hydrated cement blends in leaching environments. Specifically, the increase in total porosity and the higher solubility of Ca-depleted and highly defect C-S-H are prone to facilitate the invasion of fluids from the outer environment after initial leaching attack, like Cl^- -bearing groundwater. Such interaction can promote e.g. electrochemical corrosion of steel-reinforced concrete [10,31]. Furthermore, leaching of the cement paste, following Eq. (3)–(6), liberates alkali hydroxides, Ca^{2+} , Mg^{2+} and Al^{3+} ions, and silicic acid

into the pore solutions (see Table S1), which creates conditions suitable both for carbonation of C-S-H and precipitation of hydroxalcalite, according to Eqs. (7) and (8):



Mittermayr et al. [19] have proposed that the transformation of C-S-H into calcite generates additional pore space, which also contributes to the increase in the secondary porosity of the hydrated cement blends and especially CEM₁₀₀ (Table 3). The dissolution of portlandite alone is unlikely to generate such high porosities. This means that C-S-H decomposition generates pore space particularly in CEM₃₀/GS₇₀, CEM₉₀/SF₁₀ and CEM₁₀₀, taken the TGA results (Fig. 5 and Table 2), while all other mixes performed better. The reasons for this need further investigation, but it is reasonable that this process affects the performance of hydrated cement blends in corrosion environments. In this light, the role of hydroxalcalite should be revisited, because its formation is well-known to cause microstructural damage to the cement paste [64–66]. On the other hand, precipitation of hydroxalcalite can help preventing from steel corrosion, as this mineral phase has a high affinity to bind Cl⁻ ions [82]. Further tests utilizing analogous materials in contact with concentrated chlorine solutions will shed light on this issue.

In essence, from the datasets obtained in this study we infer that the substitution of cement by various SCMs (up to 70 wt-%) does not negatively affect the resistance of hydrated cement blends against leaching and carbonation. We refer this behavior to the different mineralogy, chemistries and microstructures developing in pure cement paste versus cement blends upon hydration, where an initially high Ca(OH)₂ content in the cement paste maintained a high pH-buffering capacity throughout (i.e. CEM₁₀₀). Substitution of hydraulically active SCMs for cement slightly reduced the Ca(OH)₂ content originally present in the cement paste due to its reaction with the SCMs to form C-S-H phases; however, strongly alkaline pore solutions (pH > 13) still evolved in all blended systems, reducing the risk of corrosion in the long term. The spatiotemporal evolution of the alteration minerals (hydroxalcalite, calcite and tobermorite-type C-S-H) that form upon leaching and carbonation, and their distribution in the cement paste, take another key control on the material's performance, i.e. either physically protecting or chemically weakening the cement paste depending on the original mix design. Probably most importantly, pure cement paste developed an open pore structure with a higher porosity, which facilitated leaching and carbonation, compared to all blended systems that generally displayed lower total porosities, denser matrices, an increased amount of chemically less reactive hydration products (mainly C-S-H) and/or inert components (e.g. micro-filler effect induced by MEF and MIF additives), making the latter mix designs less vulnerable for combined leaching and carbonation attack.

4. Conclusions

The effects of leaching and carbonation on the mineralogical, microstructural and chemical composition of hydrated cements, produced from CEM I 52.5R, and blended with high levels (up to 70 wt-%) of SCMs, have been evaluated. The following conclusions are drawn:

- (1) A sharp transitional contact zone developed between the intact inner part and the altered outer part of each mix due to leaching and carbonation front penetration. The

thickness of the altered layer reflects the degree of alteration, which was highest in pure CEM I.

- (2) Carbonation of cement clinker phases, portlandite and C-S-H resulted in the precipitation of pore-clogging CaCO₃ polymorphs, and in the development of a thin passivation layer of calcite around the leached portlandite grains. Highest CaCO₃ deposition was found in CEM I, but carbonation of C-S-H was most efficient in mixes containing GS and SF.
- (3) Portlandite, tobermorite, katoite and AFm phases disappeared towards to active leaching zone, whereas CaCO₃ phases and hydroxalcalite formed within the leached layer. The progress of these coupled dissolution/re-precipitation processes can be monitored by chemical analysis and hydrochemical modelling of expressed pore solutions.
- (4) A strong increase in pore space as well as changes in the particle form and composition of C-S-H were recognized in the altered versus unaltered paste of each mix. CEM I showed by far the highest increase in secondary porosity and the highest decrease in the Ca/Si molar ratio of C-S-H among all hydrated cement blends tested.
- (5) All hydrated cement blends performed equal or better than CEM I, also of those blends with high portion of inert fillers (MEF, MIF) of the powder, which demonstrates their at least equivalent performance in mild leaching environments. This behavior can be explained by a densification of the cement paste by reaction of Ca(OH)₂ with SCMs and by a microfiller effect, induced by optimization of the packing density of the substituents.

Declaration of Competing Interest

We declare no conflict of interests.

Acknowledgements

This work was financially supported by the NAWI Graz (Graz Advanced School of Science, GASS) and by the Austrian Research Promotion Agency (FFG, 864288). The authors would like to thank G. Brunnsteiner, D. Graf, R. Panik (all from IMBT-TVFA, TU Graz) and S. Mertschnigg (FELMI-ZFE, TU Graz) for assistance during sample production and sample preparation. The support by the lab team of the IAG (TU Graz) during preparation of samples for mineralogical, thermogravimetric, spectroscopic and chemical analyses is acknowledged. The paper benefited from the constructive comments of two anonymous reviewers.

References

- [1] V.L. Bonavetti, H.A. Donza, G. Menendez, O.A. Cabrera, E.F. Irassar, Limestone filler cement in low w/c concrete rational use of energy, *Cem. Concr. Res.* 33 (2003) 865–871.
- [2] M. Schneider, M. Romer, M. Tschudin, H. Bolio, Sustainable cement production—present and future, *Cem. Concr. Res.* 41 (2011) 642–650, <https://doi.org/10.1016/j.cemconres.2011.03.019>.
- [3] T. Proske, S. Hainer, M. Rezvani, C.A. Graubner, Eco-friendly concretes with reduced water and cement contents - Mix design principles and laboratory tests, *Cem. Concr. Res.* 51 (2013) 38–46, <https://doi.org/10.1016/j.cemconres.2013.04.011>.
- [4] S. Palm, T. Proske, M. Rezvani, S. Hainer, C. Müller, C.A. Graubner, Cements with a high limestone content - Mechanical properties, durability and ecological characteristics of the concrete, *Constr. Build. Mater.* 119 (2016) 308–318, <https://doi.org/10.1016/j.conbuildmat.2016.05.009>.
- [5] C. Shi, Z. Wu, J. Xiao, D. Wang, Z. Huang, Z. Fang, A review on ultra high performance concrete: Part I. Raw materials and mixture design, *Constr. Build. Mater.* 101 (2015) 741–751, <https://doi.org/10.1016/j.conbuildmat.2015.10.088>.
- [6] H.S. Müller, M. Haist, M. Vogel, Assessment of the sustainability potential of concrete and concrete structures considering their environmental impact, performance and lifetime, *Constr. Build. Mater.* 67 (2014) 321–337, <https://doi.org/10.1016/j.conbuildmat.2014.01.039>.

- [7] T. Proske, S. Hainer, M. Rezvani, C.-A. Graubner, Eco-friendly concretes with reduced water and cement content – Mix design principles and application in practice, *Constr. Build. Mater.* 67 (2014) 413–421, <https://doi.org/10.1016/j.conbuildmat.2013.12.066>.
- [8] E. Gartner, H. Hira, A review of alternative approaches to the reduction of CO₂ emissions associated with the manufacture of the binder phase in concrete, *Cem. Concr. Res.* 78 (2015) 126–142, <https://doi.org/10.1016/j.cemconres.2015.04.012>.
- [9] J. Carrete, S. Staquet, Monitoring and modelling the early age and hardening behaviour of eco-concrete through continuous non-destructive measurements: Part II. Mechanical behaviour, *Cem. Concr. Compos.* 73 (2016) 1–9, <https://doi.org/10.1016/j.cemconcomp.2016.07.003>.
- [10] A. Scott, M.G. Alexander, Effect of supplementary cementitious materials (binder type) on the pore solution chemistry and the corrosion of steel in alkaline environments, *Cem. Concr. Res.* 89 (2016) 45–55, <https://doi.org/10.1016/j.cemconres.2016.08.007>.
- [11] J. Juhart, G.A. David, C. Nickel, G. Fischer, F. Mittermayr, A new combined filler concept for eco-concrete, in: *Proc. 14th Int. Congr. Chem. Cem. (ICCC 2015)*, Beijing, 2015.
- [12] B. Lothenbach, K. Scrivener, R.D. Hooton, Supplementary cementitious materials, *Cem. Concr. Res.* 41 (2011) 1244–1256, <https://doi.org/10.1016/j.cemconres.2010.12.001>.
- [13] M. Antoni, J. Rossen, F. Martirena, K. Scrivener, Cement substitution by a combination of metakaolin and limestone, *Cem. Concr. Res.* 42 (2012) 1579–1589, <https://doi.org/10.1016/j.cemconres.2012.09.006>.
- [14] E. Aprianti, A huge number of artificial waste material can be supplementary cementitious material (SCM) for concrete production – a review part II, *J. Clean. Prod.* 142 (Part) (2017) 4178–4194, <https://doi.org/10.1016/j.jclepro.2015.12.115>.
- [15] F. Mittermayr, M. Rezvani, A. Baldermann, S. Hainer, P. Breitenbücher, J. Juhart, C.A. Graubner, T. Proske, Sulfate resistance of cement-reduced eco-friendly concretes, *Cem. Concr. Compos.* 55 (2015) 364–373, <https://doi.org/10.1016/j.cemconcomp.2014.09.020>.
- [16] A. Baldermann, M. Rezvani, T. Proske, C. Grengg, F. Steindl, M. Sakoparnig, C. Baldermann, I. Galan, F. Emmerich, F. Mittermayr, Effect of very high limestone content and quality on the sulfate resistance of blended cements, *Constr. Build. Mater.* 188 (2018) 1065–1076, <https://doi.org/10.1016/j.conbuildmat.2018.08.169>.
- [17] M. Romer, L. Holzer, M. Pfiffner, Swiss tunnel structures: concrete damage by formation of thaumasite, *Cem. Concr. Compos.* 25 (2003) 1111–1117. <http://www.sciencedirect.com/science/article/B6TWF-49KH0ST-1/2/fe8f87b8d6ecb8541efc38c8294de399>.
- [18] S.T. Lee, R.D. Hooton, H.S. Jung, D.H. Park, C.S. Choi, Effect of limestone filler on the deterioration of mortars and pastes exposed to sulfate solutions at ambient temperature, *Cem. Concr. Res.* 38 (2008) 68–76.
- [19] F. Mittermayr, A. Baldermann, C. Baldermann, G.H. Grathoff, D. Klammer, S.J. Köhler, A. Leis, L.N. Warr, M. Dietzel, Environmental controls and reaction pathways of coupled de-dolomitization and thaumasite formation, *Cem. Concr. Res.* 95 (2017) 282–293, <https://doi.org/10.1016/j.cemconres.2017.02.011>.
- [20] B. Słomka-Słupik, J. Podwórny, M. Staszuk, Corrosion of cement pastes made of CEM I and CEM III/A caused by a saturated water solution of ammonium chloride after 4 and 25 days of aggressive immersion, *Constr. Build. Mater.* 170 (2018) 279–289, <https://doi.org/10.1016/j.conbuildmat.2018.03.073>.
- [21] E.J. Garboczi, Microstructure and transport properties of concrete, in: J. Kropp, H. Hilsdorf (Eds.), *Rilem Rep. 12 – Perform. Criteria Concr. Durab. State Art Rep. by Rilem Tech. Comm. TC 116-PCD. Perform. Concr. as a Criterion Its Durab., E&FN Spon, 1995*, pp. 198–212.
- [22] I. Galan, A. Baldermann, W. Kusterle, M. Dietzel, F. Mittermayr, Durability of shotcrete for underground support– review and update, *Constr. Build. Mater.* 202 (2019) 465–493, <https://doi.org/10.1016/j.conbuildmat.2018.12.151>.
- [23] P. Blanc, X. Bourbon, A. Lassin, E.C. Gaucher, Chemical model for cement-based materials: thermodynamic data assessment for phases other than C–S–H, *Cem. Concr. Res.* 40 (2010) 1360–1374, <https://doi.org/10.1016/j.cemconres.2010.04.003>.
- [24] N.C.M. Marty, O. Bildstein, P. Blanc, F. Claret, B. Cochevin, E.C. Gaucher, D. Jacques, J.-E. Lartigue, S. Liu, K.U. Mayer, J.C.L. Meeussen, I. Munier, I. Pointeau, D. Su, C.I. Steefel, Benchmarks for multicomponent reactive transport across a cement/clay interface, *Comput. Geosci.* 19 (2015) 635–653, <https://doi.org/10.1007/s10596-014-9463-6>.
- [25] H.F.W. Taylor, *Cement Chemistry*, Thomas Telford, 1997. <https://books.google.at/books?id=1BOETwi7mMC>.
- [26] T. Matschei, B. Lothenbach, F.P. Glasser, The role of calcium carbonate in cement hydration, *Cem. Concr. Res.* 37 (2007) 551–558, <https://doi.org/10.1016/j.cemconres.2006.10.013>.
- [27] J. Stark, Recent advances in the field of cement hydration and microstructure analysis, *Cem. Concr. Res.* 41 (2011) 666–678, <https://doi.org/10.1016/j.cemconres.2011.03.028>.
- [28] P. Feng, C. Miao, J.W. Bullard, A model of phase stability, microstructure and properties during leaching of portland cement binders, *Cem. Concr. Compos.* 49 (2014) 9–19, <https://doi.org/10.1016/j.cemconcomp.2014.01.006>.
- [29] Y. Ouyang, X. Chen, C. Lu, J. Fang, Properties of steel fiber and macro-synthetic fiber reinforced shotcrete, *Dongnan Daxue Xuebao (Ziran Kexue Ban)/J. Southeast Univ. (Natural Sci. Ed.)*, 40 (2010) 44–48.
- [30] V.B. Duong, R. Sahamitmongkol, S. Tangtermsirikul, Effect of leaching on carbonation resistance and steel corrosion of cement-based materials, *Constr. Build. Mater.* 40 (2013) 1066–1075, <https://doi.org/10.1016/j.conbuildmat.2012.11.042>.
- [31] P. Choi, K.-K. Yun, J.H. Yeon, Effects of mineral admixtures and steel fiber on rheology, strength, and chloride ion penetration resistance characteristics of wet-mix shotcrete mixtures containing crushed aggregates, *Constr. Build. Mater.* 142 (2017) 376–384, <https://doi.org/10.1016/j.conbuildmat.2017.03.093>.
- [32] R. Boch, M. Dietzel, P. Reichl, A. Leis, A. Baldermann, F. Mittermayr, P. Pöhl, Rapid ikaite (CaCO₃·6H₂O) crystallization in a man-made river bed: Hydrogeochemical monitoring of a rarely documented mineral formation, *Appl. Geochemistry* 63 (2015) 366–379, <https://doi.org/10.1016/j.apgeochem.2015.10.003>.
- [33] J. Cowie, F.P. Glasser, The reaction between cement and natural waters containing dissolved carbon dioxide, *Adv. Cem. Res.* 4 (1992) 119–134, <https://doi.org/10.1680/adcr.1992.4.15.119>.
- [34] H.J. Wierig, Long-time studies on the carbonation of concrete under normal outdoor exposure, in: *Rilem Semin., Rilem Seminar on Durability of Concrete Structures under Normal Outdoor Exposure*, Hannover, n.d.
- [35] D.E. Macphree, H.T. Cao, Theoretical description of impact of blast furnace slag (BFS) on steel passivation in concrete, *Mag. Concr. Res.* 45 (1993) 63–69, <https://doi.org/10.1680/macrc.1993.45.162.63>.
- [36] B.G. Salvoldi, H. Beushausen, M.G. Alexander, Oxygen permeability of concrete and its relation to carbonation, *Constr. Build. Mater.* 85 (2015) 30–37, <https://doi.org/10.1016/j.conbuildmat.2015.02.019>.
- [37] A. Leemann, P. Nygaard, J. Kaufmann, R. Loser, Relation between carbonation resistance, mix design and exposure of mortar and concrete, *Cem. Concr. Compos.* 62 (2015) 33–43, <https://doi.org/10.1016/j.cemconcomp.2015.04.020>.
- [38] F.P. Glasser, J. Marchand, E. Samson, Durability of concrete – Degradation phenomena involving detrimental chemical reactions, *Cem. Concr. Res.* 38 (2008) 226–246. <http://www.sciencedirect.com/science/article/pii/S008884607002190>.
- [39] B. Bary, Simplified coupled chemo-mechanical modeling of cement pastes behavior subjected to combined leaching and external sulfate attack, *Int. J. Numer. Anal. Methods Geomech.* 32 (2008) 1791–1816, <https://doi.org/10.1002/nag.696>.
- [40] J. Wang, D. Niu, R. Ma, Y. Zhang, Investigation of sulfate attack resistance of shotcrete under dry-wet cycles, *J. Wuhan Univ. Technol. Sci. Ed.* 31 (2016) 1329–1335, <https://doi.org/10.1007/s11595-016-1535-0>.
- [41] M. Maslehuddin, M. Ibrahim, M. Shameem, M.R. Ali, M.H. Al-Mehthel, Effect of curing methods on shrinkage and corrosion resistance of concrete, *Constr. Build. Mater.* 41 (2013) 634–641, <https://doi.org/10.1016/j.conbuildmat.2012.12.064>.
- [42] E. Güneşisi, T. Özturan, M. Gesoğlu, A study on reinforcement corrosion and related properties of plain and blended cement concretes under different curing conditions, *Cem. Concr. Compos.* 27 (2005) 449–461, <https://doi.org/10.1016/j.cemconcomp.2004.05.006>.
- [43] EN 197-1, *Cement – Part 1: Composition, specifications and conformity criteria for common cements*, 2011.
- [44] A.S. El-Dieb, T.A. El-Maaddawy, Assessment of reinforcement corrosion protection of self-curing concrete, *J. Build. Eng.* 20 (2018) 72–80, <https://doi.org/10.1016/j.jobe.2018.07.007>.
- [45] J.H. Kim, S.W. Choi, K.M. Lee, Y.C. Choi, Influence of internal curing on the pore size distribution of high strength concrete, *Constr. Build. Mater.* 192 (2018) 50–57, <https://doi.org/10.1016/j.conbuildmat.2018.10.130>.
- [46] J. Tritthart, Chloride binding in cement II. The influence of the hydroxide concentration in the pore solution of hardened cement paste on chloride binding, *Cem. Concr. Res.* 19 (1989) 683–691, [https://doi.org/10.1016/0008-8846\(89\)90039-2](https://doi.org/10.1016/0008-8846(89)90039-2).
- [47] F. Mittermayr, A. Baldermann, C. Kurta, T. Rinder, D. Klammer, A. Leis, J. Tritthart, M. Dietzel, Evaporation – a key mechanism for the thaumasite form of sulfate attack, *Cem. Concr. Res.* 49 (2013) 55–64, <https://doi.org/10.1016/j.cemconres.2013.03.003>.
- [48] S. Richoz, A. Baldermann, A. Frauwallner, M. Harzhauser, G. Daxner-Höck, D. Klammer, W.E. Piller, Geochemistry and mineralogy of the oligo-miocene sediments of the Valley of Lakes, Mongolia, *Palaeobiodiversity and Palaeoenvironments* 97 (2017) 233–258, <https://doi.org/10.1007/s12549-016-0268-6>.
- [49] A. Buades, B. Coll, J.-M. Morel, A Non-Local Algorithm for Image Denoising, in: *2005 IEEE Comput. Soc. Conf. Comput. Vis. Pattern Recognit., IEEE, n.d.*: pp. 60–65. <https://doi.org/10.1109/CVPR.2005.38>.
- [50] P. Soille, *Morphological Image Analysis, 2nd ed.*, Springer Berlin Heidelberg, Berlin, Heidelberg, 2004. <https://doi.org/10.1007/978-3-662-05088-0>.
- [51] A. Baldermann, A. Griefsbacher, C. Baldermann, B. Purgstaller, I. Letofsky-Papst, S. Kaufhold, M. Dietzel, Removal of Barium, cobalt, strontium, and zinc from solution by natural and synthetic allophane adsorbents, *Geosciences* 8 (2018) 309, <https://doi.org/10.3390/geosciences8090309>.
- [52] D.L. Parkhurst, C.A.J. Appelo, *User's guide to PHREEQC (V2)*, U.S. Geol. Sur. 312 (1999).
- [53] B. Lothenbach, D.A. Kulik, T. Matschei, M. Balonis, L. Baquerizo, B. Dilnes, G.D. Miron, R.J. Myers, Cemdata18: a chemical thermodynamic database for hydrated Portland cements and alkali-activated materials, *Cem. Concr. Res.* 115 (2019) 472–506, <https://doi.org/10.1016/j.cemconres.2018.04.018>.
- [54] L. Bertolini, B. Elsener, P. Pedferri, R.B. Polder, *Corrosion of Steel in Concrete: Prevention, Diagnosis, Repair*, Wiley-VCH Verlag GmbH & Co., Weinheim, 2005.

- [55] S.E. Rasheeduzzafar, A.S. Hussain, Al-Gahtani, Pore solution composition and reinforcement corrosion characteristics of microsilica blended cement concrete, *Cem. Concr. Res.* 21 (1991) 1035–1048, [https://doi.org/10.1016/0008-8846\(91\)90064-0](https://doi.org/10.1016/0008-8846(91)90064-0).
- [56] B. Purgstaller, M. Dietzel, A. Baldermann, V. Mavromatis, Control of temperature and aqueous Mg 2+ /Ca 2+ ratio on the (trans-)formation of ikaite, *Geochim. Cosmochim. Acta.* 217 (2017) 128–143, <https://doi.org/10.1016/j.gca.2017.08.016>.
- [57] J.M. Rivas-Mercury, P. Pena, A.H. de Aza, X. Turrillas, Dehydration of Ca3Al2(SiO4)y(OH)4(3-y) (0 < y < 0.176) studied by neutron thermodiffraction, *J. Eur. Ceram. Soc.* 28 (2008) 1737–1748, <https://doi.org/10.1016/j.jeurceramsoc.2007.12.038>.
- [58] P.S. de Silva, F.P. Glasser, Phase relations in the system CaO Al2O3 SiO2 H2O relevant to metakaolin - calcium hydroxide hydration, *Cem. Concr. Res.* 23 (1993) 627–639, [https://doi.org/10.1016/0008-8846\(93\)90014-Z](https://doi.org/10.1016/0008-8846(93)90014-Z).
- [59] S.A. Bernal, J.L. Provis, B. Walkley, R.S. Nicolas, J.D. Gehman, D.G. Brice, A.R. Kilcullen, P. Duxson, J.S.J. van Deventer, Gel nanostructure in alkali-activated binders based on slag and fly ash, and effects of accelerated carbonation, *Cem. Concr. Res.* 53 (2013) 127–144, <https://doi.org/10.1016/j.cemconres.2013.06.007>.
- [60] T. Matschei, B. Lothenbach, F.P. Glasser, The AFm phase in Portland cement, *Cem. Concr. Res.* 37 (2007) 118–130, <https://doi.org/10.1016/j.cemconres.2006.10.010>.
- [61] I.G. Richardson, Tobermorite/jennite- and tobermorite/calcium hydroxide-based models for the structure of C-S-H: applicability to hardened pastes of tricalcium silicate, β -dicalcium silicate, Portland cement, and blends of Portland cement with blast-furnace slag, metakaol, *Cem. Concr. Res.* 34 (2004) 1733–1777, <https://doi.org/10.1016/j.cemconres.2004.05.034>.
- [62] E. Bonaccorsi, S. Merlino, A.R. Kampf, The crystal structure of tobermorite 14 A (Plombierite), a C-S-H Phase, *J. Am. Ceram. Soc.* 88 (2005) 505–512, <https://doi.org/10.1111/j.1551-2916.2005.00116.x>.
- [63] S. Shaw, S.M. Clark, C.M.B. Henderson, Hydrothermal formation of the calcium silicate hydrates, tobermorite (Ca5Si6O16(OH)2·4H2O) and xonotite (Ca6Si6O17(OH)2): an in situ synchrotron study, *Chem. Geol.* 167 (2000) 129–140, [https://doi.org/10.1016/S0009-2541\(99\)00205-3](https://doi.org/10.1016/S0009-2541(99)00205-3).
- [64] I.G. Richardson, A.R. Brough, G.W. Groves, C.M. Dobson, The characterization of hardened alkali-activated blast-furnace slag pastes and the nature of the calcium silicate hydrate (C-S-H) phase, *Cem. Concr. Res.* 24 (1994) 813–829, [https://doi.org/10.1016/0008-8846\(94\)90002-7](https://doi.org/10.1016/0008-8846(94)90002-7).
- [65] M. Ben Haha, G. Le Saout, F. Winnefeld, B. Lothenbach, Influence of activator type on hydration kinetics, hydrate assemblage and microstructural development of alkali activated blast-furnace slags, *Cem. Concr. Res.* 41 (2011) 301–310, <https://doi.org/10.1016/j.cemconres.2010.11.016>.
- [66] R.J. Myers, S.A. Bernal, R. San Nicolas, J.L. Provis, Generalized structural description of calcium-sodium aluminosilicate hydrate gels: The cross-linked substituted tobermorite model, *Langmuir* 29 (2013) 5294–5306, <https://doi.org/10.1021/la4000473>.
- [67] S.N. Ghosh, A.K. Chatterjee, Absorption and reflection infra-red spectra of major cement minerals, clinkers and cements, *J. Mater. Sci.* 9 (1974) 1577–1584, <https://doi.org/10.1007/BF00540754>.
- [68] S.N. Ghosh, S.K. Handoo, Infrared and Raman spectral studies in cement and concrete (review), *Cem. Concr. Res.* 10 (1980) 771–782, [https://doi.org/10.1016/0008-8846\(80\)90005-8](https://doi.org/10.1016/0008-8846(80)90005-8).
- [69] M.D. Lane, P.R. Christensen, Thermal infrared emission spectroscopy of anhydrous carbonates, *J. Geophys. Res. Planets.* 102 (1997) 25581–25592, <https://doi.org/10.1029/97JE02046>.
- [70] A. Baldermann, R. Dohrmann, S. Kaufhold, C. Nickel, I. Letofsky-Papst, M. Dietzel, The Fe-Mg-saponite solid solution series – a hydrothermal synthesis study, *Clay Miner.* 49 (2014) 391–415, <https://doi.org/10.1180/claymin.2014.049.3.04>.
- [71] M. Horgnies, J.J. Chen, C. Bouillon, Overview about the use of fourier transform infrared spectroscopy to study cementitious materials, *WIT Trans. Eng. Sci.* 77 (2013) 251–262, <https://doi.org/10.2495/MC130221>.
- [72] E. Passaglia, R. Rinaldi, Katoite, a new member of the Ca3Al2(SiO4)3-Ca3Al2(OH)12 series and a new nomenclature for the hydrogrossular group of minerals, *Bull. Minéralogie.* 107 (1984) 605–618, <https://doi.org/10.3406/bulmi.1984.7804>.
- [73] R. Žak, J. Deja, Spectroscopy study of Zn, Cd, Pb and Cr ions immobilization on C-S-H phase, *Spectrochim. Acta. Part A Mol. Biomol. Spectrosc.* 134 (2015) 614–620, <https://doi.org/10.1016/j.saa.2014.06.069>.
- [74] P. Yu, R.J. Kirkpatrick, B. Poe, P.F. McMillan, X. Cong, Structure of calcium silicate hydrate (C-S-H): Near-, Mid-, and far-infrared spectroscopy, *J. Am. Ceram. Soc.* 82 (2004) 742–748, <https://doi.org/10.1111/j.1151-2916.1999.tb01826.x>.
- [75] C.S. Walker, S. Sutou, C. Oda, M. Mihara, A. Honda, Calcium silicate hydrate (C-S-H) gel solubility data and a discrete solid phase model at 25 °C based on two binary non-ideal solid solutions, *Cem. Concr. Res.* 79 (2016) 1–30, <https://doi.org/10.1016/j.cemconres.2015.07.006>.
- [76] Z. Pavlík, A. Trník, T. Kulová, L. Scheinherrová, V. Ráhal, E. Irassar, R. Černý, DSC and TG analysis of a blended binder based on waste ceramic powder and portland cement, *Int. J. Thermophys.* 37 (2016) 1–14, <https://doi.org/10.1007/s10765-016-2043-3>.
- [77] D. Wang, C. Shi, N. Farzadnia, Z. Shi, H. Jia, Z. Ou, A review on use of limestone powder in cement-based materials: mechanism, hydration and microstructures, *Constr. Build. Mater.* 181 (2018) 659–672, <https://doi.org/10.1016/j.conbuildmat.2018.06.075>.
- [78] I. Garcia-Lodeiro, A. Palomo, A. Fernández-Jiménez, D.E. MacPhee, Compatibility studies between N-A-S-H and C-A-S-H gels. study in the ternary diagram Na2O-CaO-Al2O3-SiO2-H2O, *Cem. Concr. Res.* 41 (2011) 923–931, <https://doi.org/10.1016/j.cemconres.2011.05.006>.
- [79] J.S.J. Van Deventer, J.L. Provis, P. Duxson, Technical and commercial progress in the adoption of geopolymer cement, *Miner. Eng.* 29 (2012) 89–104, <https://doi.org/10.1016/j.mineng.2011.09.009>.
- [80] E. Ruiz-Agudo, K. Kudłacz, C.V. Putnis, A. Putnis, C. Rodríguez-Navarro, Dissolution and carbonation of portlandite [Ca(OH)2] single crystals, *Environ. Sci. Technol.* 47 (2013) 11342–11349, <https://doi.org/10.1021/es402061c>.
- [81] A. Baldermann, A. Landler, F. Mittermayr, I. Letofsky-Papst, F. Steindl, I. Galan, M. Dietzel, Removal of heavy metals (Co, Cr, and Zn) during calcium-aluminium-silicate-hydrate and trioctahedral smectite formation, *J. Mater. Sci.* (2019), <https://doi.org/10.1007/s10853-019-03541-5>.
- [82] O. Kayali, M.S.H. Khan, M. Sharfuddin Ahmed, The role of hydrotalcite in chloride binding and corrosion protection in concretes with ground granulated blast furnace slag, *Cem. Concr. Compos.* 34 (2012) 936–945, <https://doi.org/10.1016/j.cemconcomp.2012.04.009>.